Adrenergic signaling stimulates body-wide stem cell activation for limb regeneration

Duygu Payzin-Dogru[1#], Sarah E. Wilson[1#], Steven J. Blair[1], Aaron M. Savage[1], Emil Kriukov[2,3], Victor Cat[1], Louis Cammarata[4], Burcu Erdogan[1], Shifa Hossain[1], Noah Lopez[1], Julia Losner[1], Juan Velazquez Matos[1], Sangwon Min[1], Kelly Dooling[1], Bobby Groves[1], Alan Y. Wong[1], Hani Singer[1], Petr Baranov[2,3], Isaac M. Chiu[5], Brian J. Haas[6], Jessica L. Whited[1,6,7*]

[1] Department of Stem Cell and Regenerative Biology, Harvard University, Harvard University, 7 Divinity Ave., Cambridge, MA, USA, 02138
[2] Schepens Eye Research Institute of Massachusetts Eye and Ear, Boston, MA, USA, 02114
[3] Department of Ophthalmology, Harvard Medical School, Boston, MA, USA, 02114
[4] Department of Statistics, Harvard University, Cambridge, MA, USA, 02138
[5] Department of Immunology, Blavatnik Institute, Harvard Medical School, Boston, MA, USA, 02115
[6] The Broad Institute of Harvard and MIT, Cambridge, MA, USA, 02138
[7] Harvard Stem Cell Institute, Harvard University, Cambridge, MA, USA, 02138

[*] Correspondence: Jessica L. Whited, jessica_whited@harvard.edu

[#] These authors contributed equally to this work

SUMMARY

Many species throughout the animal kingdom naturally regenerate complex body parts following amputation. Most research in appendage regeneration has focused on identifying mechanisms that influence cell behaviors in the remaining stump tissue, immediately adjacent to the injury site. Roles for activation steps that occur outside of the injury site remain largely unexplored, yet they may be critical for successful regeneration. Here, we discovered a role for adrenaline in stimulating a body-wide stem cell activation response to amputation that drives limb regeneration. Notably, this systemic response is mediated by engagement of the peripheral nervous system (PNS) and adrenergic signaling at both the injury site and in distant, uninjured tissues. This work challenges the predominant conceptual framework considering the injury site alone in the regenerative response, arguing instead for body-wide stem cell activation as a priming step upon which molecular cues at the injury site then build tissue.

Keywords: regeneration, systemic responses, adrenaline, mTOR, stem cells, progenitor cells, limb, amputation

INTRODUCTION

Replacing large body parts following severe injury is a long-term goal of regenerative medicine, and one which is likely to stand on first elucidating how other animals execute this enormous task. Salamander limbs are anatomically quite similar to human limbs, yet they can be spontaneously regenerated throughout life following amputation.[1,2] Recent studies have revealed some clues about the transcriptional regulation that accompanies salamander limb regeneration, along with evidence that particular genes and molecules are important to the process.[3-7] Yet, these kinds of studies have thus far not provided critical clues about how organismal-level signaling throughout the body might be critical to regeneration. Salamanders grow an essential and outwardly-visible tissue primordium called a "blastema," which contains the progenitor cells required to grow a whole limb, while humans and other mammals do not.

Prior studies have shown that invertebrates undergo broad proliferation body-wide prior to the response becoming restricted to the site of amputation, at which point blastema formation becomes apparent.[8-11] Broad activation followed by local blastema formation as a strategy for regeneration could also underlie limb regeneration in vertebrates, but thus far this hypothesis has not been tested. If some species do use this strategy to effectively regenerate limbs, the discrete activation and blastema specification steps could be examined in detail in mammals to determine which components might occur in mammals despite their overall inability to naturally regenerate limbs. Here, we explored these concepts and effectively decoupled body-wide activation responses from subsequent blastema formation during limb regeneration. We find that injury-induced activation of adrenergic signaling critically mediates both local and systemic progenitor cell proliferation to prime body-wide tissue-resident cells for limb regeneration.

RESULTS

Amputation primes distant tissues for faster future regeneration

We recently discovered that following axolotl limb amputation, cells located throughout the body, including within contralateral unamputated limbs, proliferate, in a "systemic activation" response.[12] We also showed that systemic activation is an amputation-injury-induced response *per se*, rather than a consequence of the regeneration process, by amputating limbs and surgically blocking their regeneration.[12] Here, we first sought to understand what the consequences of systemic activation are to animals that have recently undergone amputation. We hypothesized that distant tissues harboring these systemically-activated cells might exhibit altered regeneration potentials or kinetics. We therefore challenged axolotl limbs in a systemically-active state to a local amputation 7 days later (**Figure 1A**). We found that limbs engaged in systemic activation regenerate faster than those limbs on naïve animals that had never undergone amputation (**Figure 1B-C**). We observed this effect to be significant at the early, initiation stages of regeneration (**Figure 1C**), when the blastema is being built. The effect continued through later stages of regeneration, when the blastema commences differentiation (**Figure 1D**) and digits become discernable (**Figure 1E**). We also tested whether molecular markers of blastema formation are accelerated following amputation of primed limbs versus naïve limbs. We performed HCR-FISH to detect *Prrx1* mRNA expression[13] at 5 days post-amputation (dpa) (**Figure 1F**), and we observed a significant increase in the signal intensity of this blastema-cell marker in the primed limbs versus naïve limbs (**Figure 1F-G**). This data supports the conclusion that the consequence of amputation-induced systemic activation is a priming of distant tissues for faster regeneration when subjected to future local injury.

We also investigated how many divisions cells undergo following their systemic activation and how long the priming effect lasts. Using a short-pulse (EdU) and long-chase strategy, we found most

labeled clones in limbs to be composed of 2-8 cells (**Figure 1H**), indicating amputation-induced proliferation may last only a few cell cycles. Concordantly, we found there to be no difference in the fraction of EdU+ cells by 4 weeks post-amputation (**Figure 1I**). We also found that systemically-activated limbs challenged with local amputation 4 weeks after initial activation regenerated at the same rate as naïve limbs, indicating the effect is relatively short-lived (**Figure 1J-K**).

Systemically-activated cell types are shared with proliferating cell types in homeostasis

Defining which cells are activated is key to developing hypotheses about how systemic activation relates to regeneration. We therefore asked which types of cells become systemically activated in response to amputation. Using immunohistochemistry, we also found epidermal stem cells to participate in the response (**Figure 1M**). To account for the full repertoire of activated cells that we observed, we turned to a more agnostic method of addressing this question. We used FACS and the nuclear stain Hoecsht to sort cells with 4C nuclear content from systemically-activated limbs and from homeostatic limbs (**Figure 2A-B**). We identified cell types in both samples via single-cell RNAseq and downstream clustering analyses (**Figure 2C**, **Table S1**). The distribution of marker gene expression across clusters is shown in **Figure S1A**. In the systemically-activated samples, we found multiple blood cell types, including myeloid progenitors, T cells, two clusters of hematopoietic progenitors, and two clusters of red blood cells (**Figure 2C**). We also identified skeletal muscle progenitors, two types of endothelial cells, basal epidermal cells, and four other types of epidermal cells (**Figure 2C**). Previously, we had identified satellite cells, stem cell populations that support muscle regeneration in many vertebrates,[14] as being among those cells that become activated,[12] but due to the limitations of our dissociation protocol, we did not recover them here. We parsed eight subtypes of activated fibroblasts (**Figure 2C**). Intriguingly, the same clustering algorithm applied to the 4C cells purified from homeostatic animals produced the exact same number and repertoire of cell clusters (**Figure. 2C**). This result indicates that axolotls systemically activate the same cell types that cycle during homeostasis, boosting the number of these cells actively in S-phase after amputation.

We performed differential gene expression analysis between the two conditions for each cell cluster (**Table S2**). We focused on fibroblasts because they are known to play a central role in contributing to blastema formation during limb regeneration,[15,16] and connective tissues have been shown to exhibit more plasticity across the limb regeneration process than other tissues.[17,18] We identified 19 genes to be significantly ($p<0.05$) different in expression in systemically-activated type IV fibroblasts versus 4C type IV fibroblasts from homeostatic animals (**Figure 2E**), while an additional 44 genes were differentially expressed with $0.05<p<0.1$. We detected no significant differences in gene expression in other fibroblast cell types between systemically-activated and correlating 4C cells from homeostatic animals (other than a single unannotated gene whose expression differs among the two conditions in fibroblast II). Other cell types for which we uncovered significant differential gene expression included one type of epidermal cells and one type of endothelial cells; red blood cells; myeloid progenitor and hematopoietic progenitor cells (**Figure 2D**). For the type IV fibroblasts, 8/19 genes with $p<0.05$ and 20/44 genes with $0.05<p<0.1$ are predicted to encode ribosomal subunits (**Figure 2E**, **Table S2**). 27/28 of these ribosomal subunits were more highly expressed in systemically-activated fibroblast IV cells than their 4C homeostatic counterparts. The most significant differentially expressed gene ($p<0.0059$) to display this relationship is predicted to encode Snail (**Figure 2E**), a factor most known for its promotion of epithelial-to-mesenchymal transition (EMT) in a variety of contexts,[19-21] was expressed 1.6-fold higher in systemically-activated fibroblast IV cells. We also found the p53 inhibitor Sestrin 1,[22] which also regulates mTORC1 and mTORC2 in other species by acting as a nutrient sensor,[23] to be similarly significantly upregulated ($p<0.0059$), with a 2-fold enrichment in the systemically-activated fibroblast IV cells compared to their 4C homeostatic counterparts.

To gain insights into possible cell state trajectories, we used the 4C scRNA-seq dataset to perform cell fate reconstruction analysis using RNA Velocity (**Figure 2F**).[24] In both homeostatic and systemically-activated conditions, we found evidence for fibroblast II and IV populations potentially transitioning to fibroblast I cell state, which might be enhanced in the systemically-activated samples (**Figure 2F, Figure S1C**). Genes that are most likely driving these changes are highlighted in **Figure S1D**; notably, nearly all of these genes remain unannotated in the axolotl genome, with no known high-confidence orthologs. Similarly, applying gene dynamics analysis to 4C cells dataset identified a handful of transcripts with unique regulation in the kinetics of RNA transcription and splicing (**Figure S1E**), although we again found almost all of these genes to be unannotated.

We additionally analyzed the single cells not undergoing systemic activation, those with 2C nuclear content (**Figure 2G**). We did not find any difference in the repertoire of cell types from these two conditions, 2C cells from homeostatic versus 2C cells from activated limb samples (**Figure 2G, Figure S1D**). Major transcriptional differences were observed mainly within the epidermal cell populations and small secretory cell populations (which reside in skin), indicating that a global transcriptional reprogramming of skin may occur downstream of amputation (**Figure 2H, Table S3**). Collectively, the data indicate that amputation induces a subset of cell types throughout the body that ordinarily can proliferate during homeostasis to become hyper-proliferative, thus becoming systemically activated.

mTOR signaling is required for systemic activation and priming

Our previous work demonstrated that mTOR signaling is upregulated in distant tissues, such as contralateral limbs, during systemic activation.[12] We find this interesting because this pathway can be activated following injury in mice[25,26] despite the fact that they do not regenerate limbs. Additionally, we used CellChat[27] and our scRNA-seq dataset to identify possible signaling pathways that may drive differences between 4C cells in the systemically-activated versus homeostatic conditions, and we found substantial differences in Hepatocyte growth factor (HGF) signaling, which acts to stimulate mTOR signaling in mice and in human cells (**Figure 3A**).[25,26,28] We therefore tested whether axolotls use mTOR signaling for systemic activation and priming. We treated axolotls with the mTOR inhibitor rapamycin,[29] and we found that rapamycin wholly blocked systemic activation of cells in contralateral limbs, as indicated by significantly fewer EdU+ nuclei (**Figure 3B-C**). This finding led us to ask if mTOR signaling is also required for priming of distant tissues for faster regeneration. We tested this hypothesis (**Figure 3D**), and we found that mTOR signaling is required for priming axolotl limbs for faster regeneration following amputation elsewhere (**Figure 3E**). This requirement is evident both at the early stages of blastema initiation (**Figure 3F**) and at later stages when limbs start to differentiate (**Figure 3G**). Separately, we also asked whether mTOR is required for limb regeneration, in the context of a single amputation. We found that treating axolotls with rapamycin for a time period of two days prior to through 7 days after limb amputation led to a diminished rate of early blastema growth (**Figure S2A-B**), but, ultimately, these limbs regenerated and were outwardly normal at 10 weeks post-amputation (**Figure S2C**). While mTOR activation in mice has been shown to be mediated via molecular messengers in the circulation,[25,26] we were interested in understanding whether mTOR signaling may be activated within the nervous system to regulate systemic activation in axolotls. We examined mTOR activation in dorsal root ganglia (DRG), which include somatosensory neurons that innervate and receive sensory input from the limbs as well as non-neuronal cells such as fibroblasts and satellite glia (**Figure 3H**).[30] While there was no significant difference in the proliferation of cells in the DRGs following amputation (**Figure 3I**), we found that DRGs from both amputated limbs and contralateral limbs showed higher levels of mTOR activation as indicated by pS6+ cells than those from homeostatic animals (**Figure 3J**).

Peripheral nervous system is a conduit for systemic proliferative response to amputation

Determining the mode by which amputation-induced signals spread throughout the body is important for unraveling the molecular mechanisms of the systemic activation response. We hypothesized that the peripheral nervous system (PNS) might be a conduit for this type of information, as it transduces sensory information to the brain and spinal cord, thereby facilitating communication between distant locations in the body. This hypothesis was strengthened by the upregulation in mTOR signaling in DRGs we observed after amputation. We tested whether systemic activation requires peripheral innervation at either the responding site (**Figure 4A-C**) and/or the amputation site (**Figure 4D-F**) using surgical denervation. We found that systemic activation did not occur when these distant sites were denervated at the time that contralateral limbs were amputated (**Figure 4A-C**). As a control, we found systemic activation still occurred following amputation when these distant sites (contralateral limbs) underwent sham operations. We parsed the contralateral tissues into three broad bins—epidermis, skeletal elements, and internal (non-skeletal, soft) tissues—and quantified the extent of systemic activation within each (**Figure 4D-F**). This analysis revealed each of these three bins of tissue types requires innervation for cellular activation. We also found that when limbs were denervated then immediately amputated, the amputation no longer provoked systemic activation in distant sites (contralateral limbs) (**Figure 4G-I**). Sham surgeries in which limbs were not denervated prior to their amputation still provoked the systemic activation response. These results demonstrate that peripheral innervation of both the amputated limb and the distantly-responding limb are required for systemic activation of progenitor cells. Therefore, both neuronal input that senses injury and neuronal output that mediates efferent signaling to tissues could regulate systemic activation. To explore molecular pathways that may underlie PNS dependence in responding tissues, we performed two types of bulk RNA-seq analyses. We compared gene expression in limb nerve bundles from animals actively engaged in systemic activation to those who failed to systemically activate due to denervation (**Figure 4J**). We identified 273 genes with substantially different expression between these two conditions (**Figure 4J**, **Table S5**). We also performed differential gene expression analysis between samples derived from the soft tissue of systemically-activated limbs and the soft tissue of limbs that were denervated and therefore not activated (**Figure 4K**). This analysis identified 82 differentially-expressed genes (**Figure 4K**, **Table S5**).

a-Adrenergic signaling drives systemic activation and priming

We next used the candidate genes revealed by the RNA-seq of nerve and surrounding tissue to functionally test pathways to determine if they are required for systemic activation. We prioritized well-studied pathways with robust pharmacological inhibitors. *Adra2a*, which encodes a-2A adrenergic receptor, was 7.4-fold upregulated in transected nerve samples, which are deficient in stimulating systemic activation, compared to intact nerves (**Figure 4J**, **Table S5**), implicating a possible role for adrenergic signaling in the systemic activation response to amputation. Separately, we investigated adrenergic receptor signaling in our scRNA-seq dataset, and we found many adrenergic receptors to be widely expressed in both homeostasis and activated conditions (**Figure S3**). The primary neurotransmitter mediators of adrenergic signaling are the stress-related hormones epinephrine and norepinephrine.[31] We therefore quantified levels of these molecules in axolotl plasma using ELISA. We found that while circulating levels of norepinephrine are similar between unamputated axolotls and axolotls at four hours post-amputation (**Figure 5A**), the amputated animals exhibited approximately 2-fold more epinephrine in plasma (**Figure 5B**). To address function, we treated axolotls with yohimbine, a well-studied Adra2a antagonist,[32,33] to test for an adrenergic signaling requirement in systemic activation. We found that in animals treated with yohimbine, limbs contralateral to amputation did not undergo systemic activation, demonstrating that adrenergic signaling is required for systemic stem cell activation in response to amputation (**Figure 5C-D**). We then asked whether adrenergic signaling is also required for priming distant tissues for future regeneration (**Figure 5E**). We found that when axolotls were treated with yohimbine through the time period 2 days before to 7 days after amputation, priming was diminished

(**Figure 5F**), with both initial blastema growth (**Figure 5G**) and limb differentiation (**Figure 5H**) occurring more slowly. We tested whether stimulating adrenergic signaling via the agonist clonidine might enhance priming (**Figure 5I**), and we found evidence that this pathway can indeed be stimulated to accelerate the regeneration of distant tissues that have been systemically activated (**Figure 5J-K**). Our finding that a2-adrenergic-receptor signaling mediates systemic activation prompted us to ask whether b-adrenergic-receptor signaling also contributes to systemic activation. We therefore used an identical treatment regimen to administer the non-selective b-adrenergic receptor antagonist propranolol [34] to axolotls (**Figure 5L-N**). We found that while propranolol treatment led to a significantly decreased fraction of cells actively in S-phase within blastemas of regenerating limbs (**Figure 5L-M**), it had no effect on systemic activation (**Figure 5L, 5N**). These results indicate that a-adrenergic signaling is required for the systemic activation response to amputation in axolotls, but b-adrenergic signaling is only required for the localized cellular proliferation response at the amputation site.

In parallel, we also tested whether systemic activation requires insulin and Wnt signaling as both Igfr1 and Lef1 were differentially regulated (in surrounding tissue and nerves, respectively) in denervated limbs versus sham-operated limbs following amputation **(Table S5**). CellChat analysis also supported differential regulation of Insulin/IGF signaling between homeostatic and activated states in the 4C populations (**Figure S4A-B**). Inhibition of Igf1r by NVP-ADW742,[35] an ATP-competitive inhibitor, blocked systemic activation in limbs contralateral to amputation, indicating Igf-1 signaling is also necessary for this process (**Figure S4 C-D**). Although Wnt signaling has been implicated in a variety of regenerative events across many species,[36-40] we found it to be dispensable for systemic activation in axolotl as the Wnt inhibitor IWR-1[41] did not alter the number of cells that become systemically activated in response to amputation (**Figure S4**).

Chromatin accessibility changes associated with systemic activation

We hypothesized that cells might be altering their chromatin accessibility in response to amputation injury as a means to shift into an activated state, primed for regeneration. To address this possibility, we used our FACS strategy to isolate 4C cells from the homeostatic limb, systemically-activated limb, and regenerating limb samples including the blastema and wound epidermis. We pooled cells from each of these three conditions and performed ATAC-seq, and we identified 140 regulatory regions across 119 genes (**Figure 6**). Principal component analysis of these three populations revealed that the three conditions cluster separately with respect to PCA 1 and 2 (**Figure 6A**).

Most peaks with differential accessibility mapped to unannotated genes (**Figure 6B**). However, we uncovered several differences in chromatin accessibility near or within annotated genes across the three conditions. For example, we only recovered peaks from 4C cells isolated from systemically-activated limbs, but not 4C cells from homeostatic or regenerating samples for *Foxo1* (**Figure 6C**). We also found *Dyrk2* loci to be more accessible in the activated 4C samples compared to 4C homeostatic and blastema samples (**Figure 6C**). DYRK2 is a direct downregulator of two key regulators of G1/S transition, c-JUN and c-MYC, suggesting that it might be involved in maintaining the stem cells of the activated limbs in a quiescent state.[42] These data suggest chromatin may be opened in the vicinity of genes key for regulating the systemically-activated state, while it may be closed when cells proliferate during homeostasis and while in the blastema cell state.

DISCUSSION

Our results highlight a previously-unappreciated role for body-wide activation of cell types that cycle during organismal homeostasis and their repurposing for pro-regenerative responses during

vertebrate limb regeneration. Our data support a model in which the mechanism of systemic activation requires peripheral innervation at both the injury and distant responding sites. Our work identifies a more primary role for peripheral innervation in the initial stimulation of progenitor cells to re-enter the cell cycle. This role for PNS is complementary to the previously-appreciated roles for PNS as a source of mitogens in growing nascent blastemas to become larger[43-47] and as a positive regulator of limb size during regeneration.[48] We investigated the mechanisms whereby systemic activation occurs, and we discovered adrenergic signaling and mTOR pathways as critical mediators of both systemic activation and priming for future regeneration.

Our work provides molecular support for vertebrate limb regeneration being predicated on the activity of cells with shared use during homeostasis. Future studies will be required to understand the downstream pathways that these cells use to become poised to promote limb regeneration following an amputation. How cells sense their location in space and respond accordingly may depend on their proximity to other extrinsic cues, such as the wound epidermis that forms specifically at the injury site. We postulate that while the initial proliferative response to amputation is global in axolotls **(Figure 6E),** the sustained proliferation of activated cells and their migration out of tissue niches may be driven by wound-epidermis factors. This prediction aligns with the finding that suturing salamander limbs closed after amputation blocks formation of this molecularly-specialized, transient wound epidermis and, thus, outward blastema formation.[49] However, when sutures were removed after 5 weeks, the wound epidermis formed and limbs grew visible blastemas and fully regenerated—at a faster rate than a fresh amputation.[49] In essence, this experiment temporally decoupled the amputation injury from blastema formation, and suggesting that cells may have been poised by the injury and held in that state until receiving signals from wound epidermis. Our study provides molecular support for this model.

Several outstanding questions remain for understanding the implications of our findings. Additional experimentation will be required to address the relative contributions of sympathetic neurons locally versus the hypothalamic-pituitary-adrenal (HPA) axis as the source of the catecholamines important for regeneration. While we showed that the systemic activation and priming effects are transient, and that they disappear within several weeks, the mechanism whereby they are extinguished remains to be determined, and the determining the role of epigenetics in this process requires more experimentation. Our ATAC-seq analysis identified the promoter region of the *Dyrk2* loci to be more accessible in the 4C cells of the activated limb compared to homeostatic limbs, suggesting this kinase could be important to keep the activated stem cells in a quiescent state in the absence of injury-site specific signals to commit to a blastema cell fate. We also identified loci of interest whose homologs have relevance to stem cell populations in other species. For example, Tetraspanins have been implicated as markers of planarian neoblast subsets with enhanced differentiation potentials,[50] and FOXO1 is required to maintain pluripotency in human embryonic stem cells.[51] Importantly, the fork head transcription factors act downstream of insulin signaling to promote longevity and cell survival,[52,53] in line with our findings that suggest insulin/IGF1R signaling is required for systemic activation (**Figure 4S**). Addressing hypotheses about how the cells we have identified in axolotl might relate to planarian neoblasts and mammalian stem cells will require additional experimentation. Additionally, while systemic activation may have short-term benefits to the organism by acting to prime other tissues for regeneration, the consequences of this system over the individual lifespan need to be evaluated. Repeated injury and chronic stimulation of this system may come at a cost. While we can imagine scenarios whereby coupling systemic activation to limb regeneration might be evolutionarily advantageous, for example in high-density settings among cannibalistic species,[54] addressing these possibilities will require controlled experimentation.

Our work is likely to have important implications for defining where in the process of limb regeneration mammals have evolved and/or retained additional molecular controls that restrict natural regenerative ability. As mice have been shown to engage in a similar response following more limited local injuries,[25] the possibility that the first step of limb regeneration—in which cycling progenitor cells shift from a homeostatic function to a regenerative function—is operational and salient in mammals. Whether

an important role for the peripheral nervous system in orchestrating the body-wide activation response in mammals also exists, perhaps intertwined with the circulation, remains to be determined. Additional studies will also be required to reveal if either, or both, axolotls and mice reserve some subset of these homeostatic progenitor cell types exclusively or preferentially for regeneration. Elucidating how some of these activated progenitors enter the blastema cell state will be critical. Our work predicts that activating the relevant cell types and directing them toward a regenerative response could be stimulated by harnessing adrenergic and mTOR signaling in a mammalian setting, providing a major advancement toward the goal of therapeutic limb regeneration in the future. Our findings may also provide important reference points for medical applications outside of the amputee population, for example, in the context of "polytrauma," in which a patient suffers severe wounds in several different body parts.[55]

ACKNOWLEDGMENTS

This work was supported by The Richard and Susan Smith Family Odyssey Award (J.L.W.), the NIH New Innovator Award DP2HD087953 (J.L.W.), NICHD R01HD095494 (J.L.W.), NSF-CAREER award (J.L.W.), Harvard University Faculty of Arts and Sciences (J.L.W.), Harvard/MIT Joint Basic Program in Neuroscience (J.L.W. and I.M.C.), the Human Frontiers Science Program Long-term Postdoctoral Fellowship (A.M.S.), the Harvard Program for Research in Science and Engineering (S.H. and J.L.), the Harvard College Research Program (S.H. and A.Y.W.), and the Harvard Stem Cell Institute (A.W.). We thank Dr. Elaine Fuchs' lab for sharing reagents. We thank Samantha Payne, Solsa Cariba, Sydney Chambule, Jason Buenrostro, Fabiana Duarte, Juliana Babu, Jeramiah Smith, Nataliya Timoshevskaya, Tomás Gomes, and Adnan Abouelela for technical assistance. We thank William Ye, Tyler Mourey, and Quinley Miao for animal care. We thank Ya-Chieh Hsu, Matthew Warman, Marc Kirschner, Davie Van Vactor, Paola Arlotta, Rich Lee, Paul Garrity, and members of the Whited, Chiu, Greer and Lehoczky labs for discussions and comments on the manuscript. We thank Yulia Swartz for sharing reagents and assisting in data interpretation, and the Bauer Core Facility at Harvard University for cell sorting and sequencing.

AUTHOR CONTRIBUTIONS

D.P.-D, S.E.W., B.E., S.H., J.L., J.V.M, I.M.C., and J.L.W. designed the experiments; D.P.-D. S.E.W., and J.L.W. wrote the paper; S.J.B. , E.K., and B.J.H. designed and performed computational analyses; L.C. performed statistical analyses; D. P.-D., S.E.W., A.M.S., B.E., N.L., S.M., B.G., K.D., S.H., J.V.M., A.W., J.L., and H.S. performed sample preparation, experiments, and experimental data analyses. All authors contributed to manuscript editing.

DECLARATION OF INTERESTS

JLW is a co-founder of Matice Biosciences. Other authors declare no competing interests.

MAIN FIGURE TITLES AND LEGENDS

Figure 1. Systemically-activated cells are primed for future regeneration events.
(A) Experimental design. We compared regeneration rates of systemically-activated and naïve, control limbs. Green dots, activated, EdU positive nuclei. **(B)** Representative images of regenerating systemically-activated or control limbs. **(C-E)** Quantification of blastema area at 14 dpa **(C)**, differentiating

limbs **(D),** and number of digit outlines **(E)** at 25 dpa (n=15 animals for each condition in blastema area measurement, n = 30 limbs for each condition in differentiation and digit outline quantification). **(F)** *Prrx1* HCR-FISH was performed on tissue sections at 5 dpa following local amputation of naïve limbs (no previous amputation) and primed limbs (previously amputated on the contralateral side 14 days earlier). **(G)** Quantification of *Prrx1* mean fluorescence intensity across entire tissue sections (n = 8 animals for each group). **(H)** EdU and DAPI staining of intact limbs (left) and limbs contralateral to amputation (right) harvested 6 weeks after EdU administration. **(I)** Quantification of percent EdU positive nuclei of intact and contralateral limbs in **(H),** (n = 15 animals for intact and n = 12 animals for contralateral group). **(J)** Representative images of systemically-activated and naïve limbs amputated 28 days post-contralateral amputation. **(K-L)** Quantification of blastema area at 7 dpa **(K)** and number of digit outlines at 27 dpa **(L)** (n = 19 animals for control, n = 20 animals for activated for blastema area measurement, n = 38 limbs for control and n = 40 limbs for systemically-activated animals in digit outline quantification). **(M)** Keratin 5 (left), Keratin 10 (right) staining of limbs contralateral to amputation harvested 12 and 14 days post-amputation, respectively, 18 hours after EdU administration. All data shown as mean ± SD. Statistical significance was determined using unpaired two-tailed Welch's t-test in **(C)**, **(G)**, **(I)** and **(K)**; Fisher's exact test in **(D)**; and Fisher's exact test with Freeman-Halton extension in **(E)** and **(L).** Scale bars, 2 mm in **(B)** and **(D)**; 500 µm in **(H)**; 200 µm in **(M).** dpa, days post-amputation. K5, keratin 5. K10, keratin 10. EdU, 5-ethynyl-2′- deoxyuridine.

Figure 2. Systemically-activated cells represent the same broad cell types as cells proliferating during homeostasis. (A) Experimental design to identify systemically activated cells and compare to proliferating cells during homeostasis. Dividing (4C) cells of systemically-activated and naïve, control limbs were isolated by sorting dissociated cells according to their DNA content. **(B)** Representative FACS distribution following Hoecsht stain of homeostatic and systemically-activated limb cell samples. **(C)** UMAP plot of 4C cells collected from homeostatic control limbs (n = 4) and systemically-activated limbs (n = 4). **(D)** Heat map depicting statistically-significant differential gene expression between 4C cells in homeostatic versus activated samples. Only cell types with differential gene expression are shown. **(E)** Dot plot showing relative frequency of expression (dot size) and expression level (color) for differentially expressed genes across the eight fibroblast cell populations in homeostatic (H) versus activated (A) samples. **(F)** Cell fate reconstruction analysis of 4C cells in homeostatic and systemically activated limbs. **(G)** UMAP plot of 2C cells collected from homeostatic control limbs (n = 3) and systemically-activated limbs (n = 4). **(H)** Heat map depicting statistically-significant differential gene expression between 2C cells in homeostatic versus activated samples. Only cell types with differential gene expression are shown. See also **Figure S1.**

Figure 3. mTOR signaling is required for systemic activation and priming. (A) Chord diagrams of CellChat analysis of HGF signaling between cell types identified by scRNA-seq in Figure 2. **(B)** pS6 and EdU staining of blastema, intact (homeostatic) and contralateral limb tissue sections from animals treated with saline, vehicle, or rapamycin at 14 dpa. **(C)** Quantification EdU positive nuclei at 14 dpa (n = 12 limbs for intact saline, intact vehicle and intact rapamycin groups, n = 10 limbs for amputated saline and amputated vehicle, and n = 8 limbs for amputated rapamycin group). **(D)** Experimental design to test requirement for mTOR in priming. Animals were treated with rapamycin or vehicle solution by daily injections starting from 3 days before to 7 days post unilateral amputations. The treatments were then ceased, and the uninjured contralateral limbs were unilaterally amputated. The regeneration rates of the second set of amputations were compared between treatment groups. **(E)** Representative images of regenerating contralateral limbs of rapamycin and vehicle solution-treated animals. **(F)** Quantification of blastema area at 7 days post-amputation. **(G)** Quantification of the number of digit outlines at 23 days post-amputation (n=20 animals for vehicle and rapamycin; n = 40 limbs for vehicle and rapamycin for each condition in digit outline quantification). The same group of vehicle control animals were used in Figure 5 (I-J). **(H)** pS6 and EdU staining of dorsal root ganglia servicing homeostatic, amputated, and contralateral limbs at 7 days post amputation (n = 20 for homeostatic and amputated, and n = 18 for contralateral). **(I-J)** Quantification of EdU positive **(I)** and pS6 positive **(J)** nuclei for DRGs in **(H)**. All data shown as mean ± SD. Statistical significance was determined using unpaired two-tailed Welch's t-test

with Bonferroni-Dunn correction in **(C)**; two-tailed Welch's ANOVA with Dunnett's T3 correction for multiple hypothesis testing in **(F)**, **(I)** and **(J)**; and Fisher's exact test with Freeman-Halton extension in **(G)**. Scale bars, 500 μm in **(B)**; 2 mm in **(E)**; and 100 μm in **(H)**. rapa, rapamycin. Int, intact. contra, contralateral. dpa, days post-amputation. pS6, phospho-S6 ribosomal protein; EdU, 5-ethynyl-2′-deoxyuridine. See also **Figure S2, Tables S1-S4.**

Figure 4. PNS at both amputation site and responding site are required for systemic activation and priming. **(A)** Experimental design. Nerve bundles innervating limbs contralateral to unilateral amputations were transected or sham-operated, and animals were assayed for systemic activation. Animals receiving unilateral denervations or sham-operations with no amputations were used as controls. **(B)** EdU and DAPI staining of intact and contralateral limb tissue sections of denervated and sham-operated animals in the intact state or at 14 days post amputation. **(C)** Quantification of percent EdU positive nuclei in denervated and sham-operated at 14 dpa. **(D-F)** Breakdown of tissue types represented in **(C)**. **(D)** Epidermis. **(E)** Skeletal elements. **(F)** Internal, non-skeletal tissues. (n = 11 animals for sham, n = 10 animals for denervated, n = 13 animals for sham amputated and denervated amputated, **(G)** Experimental design. Nerve bundles were transected or sham-operated in limbs that were immediately amputated thereafter. **(H)** EdU and DAPI staining of intact and contralateral limb tissue sections of denervated and sham-operated animals in the intact state or at 14 days post amputation. **(I)** Quantification of percent EdU positive nuclei in denervated and sham-operated at 14 dpa. (n = 18 animals for sham, n = 16 for sham amputated, n = 11 for denervated, and n = 12 for denervated amputated. **(J-K)** Differential gene expression analysis identifies transcripts that are enriched in nerve ends **(J)** and responding tissues **(K)**. All data shown as mean ± SD. Statistical significance was determined using unpaired two-tailed Welch's t-tests with Bonferroni-Dunn correction. Scale bars, 500 μm. den, denervated. int, intact. contra, contralateral. EdU, 5-ethynyl-2′-deoxyuridine. See also **Table S5**.

Figure 5. α-Adrenergic signaling is required for systemic activation and priming. **(A)** Plasma levels of norepinephrine at homeostasis and 4 hours post-amputation, as determined by ELISA. **(B)** Plasma levels of epinephrine at homeostasis and 4 hours post-amputation, as determined by ELISA. **(C)** EdU and DAPI staining of limbs contralateral to unilateral amputations treated with yohimbine or vehicle control, harvested at 7 days post amputation. **(D)** Quantification of percent EdU positive nuclei in contralateral limbs in **(C)** (n = 15 animals for each group, analyzed by unpaired two-tailed Welch's t-test). All data shown as mean ± SD. Scale bar, 500 μm. EdU, 5-ethynyl-2′-deoxyuridine. **(E)** Experimental design. Animals were treated with Adra2a inhibitor yohimbine or vehicle solution by daily injections starting from 2 days before to 7 days post unilateral amputations. The treatments were then ceased, and the uninjured contralateral limbs were unilaterally amputated. The regeneration rates of the second set of amputations were compared between treatment groups. **(F)** Representative images of regenerating contralateral limbs of yohimbine and vehicle solution treated animals. **(G)** Quantification of blastema area at 14 days post-amputation (n=15 animals for each condition). **(H)** Quantification of the number of digit outlines at 25 days post-amputation (n = 30 limbs for each condition). **(I)** Experimental design. Animals were treated with Adra2a agonist clonidine or vehicle solution by daily injections starting from 3 days before to 7 days post unilateral amputations. The treatments were then ceased, and the uninjured contralateral limbs were unilaterally amputated. The regeneration rates of the second set of amputations were compared between treatment groups. **(J)** Representative images. **(K)** Quantification of blastema area at 7 days post-amputation. (n = 20 animals for vehicle and n = 18 animals for clonidine). The same group of vehicle control animals were used in Figure 3 (E-G). **(L-N)** EdU and DAPI staining of limbs contralateral to unilateral amputations treated with propranolol or vehicle control, harvested at 7 days post-amputation. **(L)** Representative images. **(M)** Quantification of percent EdU positive nuclei within the blastema area of the initially-amputated limbs (n = 15 animals for vehicle and n = 10 for propranolol). **(N)** Quantification of percent EdU positive nuclei within contralateral limbs (n = 15 animals for vehicle and n = 10 for propranolol). Statistical significance was determined using paired two-tailed Welch's t-tests in **(A)** and **(B)**; unpaired two-tailed Welch's t-tests in **(D)**, **(G)**, **(M)** and **(N)**; Welch's ANOVA with Dunnett's T3 correction in **(K)**; Fisher's exact test with Freeman-Halton extension in **(H)**. Scale bars, 500 μm in **(C)** and **(L)**; 2 mm in **(F)** and **(J)**. hpa, hours post-amputation. dpa, days post-amputation. YOH, yohimbine. See also **Figure S3**.

Figure 6. (A) Principal component analysis of chromatin accessibility of 4C cells in homeostatic, activated, and regenerating limbs. **(B)** Heatmap showing relative abundances accessible regions in 4C cells of homeostatic, activated, and regenerating limbs. **(C-D)** Genome browser tracks showing accessible regions of the Foxo1 **(C)** and Dyrk2 **(D)** loci. **(E)** Two-step model for blastema cell specification. In step 1, some cells (magenta nuclei) from a field of possible progenitor cells re-enter the cell cycle (activation) and begin to proliferate in response to amputation. We postulate this step is systemic, occurring throughout the body. In step 2, some subset of activated progenitor cells later converts to the blastema cell state (blue cells). We postulate this step is local to the site of amputation. The subsequent migration of blastema cells to the distal-most tip of the stump creates a visible blastema (yellow).

STAR Methods

RESOURCE AVAILABILITY

Lead contact

Further information and requests for resources and reagents should be directed to and will be fulfilled by the lead contact, Jessica Whited (jessica_whited@harvard.edu).

Materials availability

This study did not generate new unique reagents.

Data and code availability

- All bulk RNA-sequencing data sets generated during this study are available at Gene Expression Omnibus (GEO), accession number GSE192477.
- All single-cell RNA-sequencing datasets generated in this study are available at Gene Expression Omnibus (GEO), accession numbers GSE232083 (4C) and GSE232082 (2C).
- All bulk ATAC-sequencing datasets generated in this study are available at Gene Expression Omnibus (GEO), accession number GSE232080.
- All original code has been deposited at Zenodo and is publicly available as of the date of publication. The DOI is listed in the key resources table.
- Any additional information required to reanalyze the data reported in this paper is available from the lead contact upon request.

EXPERIMENTAL MODEL AND SUBJECT DETAILS

Animals

All animal experimentation was approved by and conducted in accordance with Harvard University's Institutional Animal Care and Use Committee. Leucistic axolotls were used for all animal experimentation except RNA sequencing and maintained as previously described.[5] For RNA sequencing, *βIIItub:GAP43-EGFP* transgenic animals were used.[56] Animals in all experiments were both age and size matched. Animals were anesthetized in 0.1% (w/v) tricaine prior to all procedures involving amputation, denervation, or injection. After all surgical procedures, axolotls were allowed to recover overnight in 0.5% (w/v) sulfamerazine. All limb amputations were performed at the mid-stylopod and the bone was then trimmed back from the amputation plane. For forelimb denervations the brachial plexus nerves were transected as described previously,[57] and for hindlimb denervations the sciatic nerves were transected as described[58]. Sham operations as controls for denervations were performed by anesthetizing animals and

cutting the skin open with sterile scissors, locating the nerve bundles with closed sterile forceps, but not cutting the nerves.

METHOD DETAILS

Denervations and amputations

Animals in all experiments were both age and size matched. Animals were anesthetized in 0.1% (w/v) tricaine prior to all procedures involving amputation, denervation, or injection. After all surgical procedures, axolotls were allowed to recover overnight in 0.5% (w/v) sulfamerazine. All limb amputations were performed at the mid-stylopod and the bone was then trimmed back from the amputation plane. For forelimb denervations the brachial plexus nerves were transected according to Schotté *et al.* [57] and for hindlimb denervations the sciatic nerves were transected according to Kropf *et al.* [58] Sham operations as controls for denervations were performed by anesthetizing animals and cutting the skin open with sterile scissors, locating the nerve bundles with closed sterile forceps, but not cutting the nerves.

Drug treatments and EdU incorporation

Rapamycin was dissolved into a 25 mg/ml stock solution in ethanol. Rapamycin treatments were delivered via both water treatments at a concentration of 1 μM for 16 days with water changed daily, and through daily intraperitoneal injections at a concentration of 5 mg/kg/day for 16 days, both starting two days before amputation. All intraperitoneal injections were administered at a volume of 20μL/g in a vehicle solution comprised of APBS with 5% Tween80, 5% PEG-400. All stock solutions were frozen at −80 °C in 1-mL aliquots. Yohimbine (Y3125, Sigma-Aldrich) was dissolved into a 10 mg/mL stock solution with sterilized water. Yohimbine was administered daily at a dose of 1mg/kg for 14 days via intraperitoneal injection. A stock solution of IWR-1 (I0161, Sigma-Aldrich) was created by dissolving 5mg/mL in DMSO. IWR-1 was delivered daily at a dose of 10mg/kg/day for 9 days via intraperitoneal injection. A stock solution of NVP-ADW742 (5247, Tocris) was created by dissolving 2mg/mL in DMSO. NVP-ADW742 was injected daily at a dose of 10mg/kg/day for 14 days. Clonidine (C7897, Sigma-Aldrich) was dissolved in water at 7.5 mM stock concentration and was delivered via water treatments at 30 μM. A stock solution of propranolol (P0884, Sigma-Aldrich) was created by dissolving 100 mM in water. Propranolol was delivered via water treatments at 5 μM. 5-ethynyl-2′-deoxyuridine (EdU) was purchased from ThermoFisher and stock solutions were created by dissolving the powder in dimethyl sulfoxide as instructed by the manufacturer. Following anesthetization, axolotls were administered 20 μL/g of 400 μM EdU in 0.7X PBS via intraperitoneal injection 18 hours before tissue harvest.

Skeletal and tissue preparations

For tissue sections, post-collection, tissue samples were fixed in 4% paraformaldehyde in DEPC-treated PBS overnight at 4°C. Tissues were then cryopreserved in a sucrose gradient following a wash in DEPC-PBS and incubated in 30% sucrose/DEPC-PBS at 4°C overnight. Tissues were then embedded and frozen on dry ice in Tissue-Tek O.C.T. Compound (Sakura) and stored at −80°C. All blocks were sectioned at 16μm thickness using a Leica CM 1950 cryotome and sections were stored at −80°C until use.

For skeletal preparations, post-collection, limbs were incubated overnight in 95% ethanol at room temperature and then incubated in 100% acetone under the same conditions. Skeletal elements were visualized with alcian blue and alizarin red S stains followed by a clearing of non-skeletal tissue with potassium hydroxide.

590 **Immunofluorescence and HCR-FISH**
591 Sections were rehydrated with PBS and then permeabilized with 0.5% Triton-X-100 PBS. Post-
592 permeabilization, slides were rinsed twice with PBS and EdU visualization was performed via sulfo-
593 cyanine 3 azide (Lumiprobe). Post-EdU visualization slides were washed twice with PBS. Staining and
594 labeling with any additional antibodies was conducted post-EdU labeling. Primary antibodies used were
595 rabbit anti-phospho-S6 ribosomal protein (Ser235/236, 1:200; Cell Signaling 4858), and rabbit anti-keratin
596 10 (BioLegend 905401). Secondary antibodies used were Cy3-goat anti-mouse (1:250, Jackson
597 ImmunoResearch 115-165-146), Alexa Fluor 488-Goat Anti-Rabbit (1:250, Jackson ImmunoResearch,
598 111-545-003) and Cy3-goat anti-rabbit (1:250, Jackson ImmunoResearch 111-165-003).
599
600 Sections stained with all antibodies were blocked with 10% serum from the host species of the secondary
601 antibody in 0.1% Triton-X-100 in PBS. Primary and secondary antibodies were diluted in in 2% BSA,
602 0.1% Triton-X-100 in PBS. Sections labeled with anti-pS6 and NeuN underwent an antigen retrieval step
603 after permeabilization, in which slides were boiled in 0.1 M sodium citrate (pH 6.0) and then rinsed once
604 in PBS, before EdU was visualized, followed by blocking and primary antibody incubation. All slides were
605 incubated with DAPI (Sigma D9542) before cover slipping. HCR-FISH was performed as described
606 previously.[59]
607
608 **Plasma isolation and ELISA**
609 Blood was collected from axolotls as described previously.[60] Efferent blood vessels were exposed by
610 placing the animals on its back. Winged infusion sets were used to collect the blood. Whole blood was
611 placed into EDTA coated tubes and spun down. The supernatant fraction (plasma) was used for
612 downstream analysis. Animals were allowed to recover overnight in fresh axolotl water. Epinephrine and
613 norepinephrine ELISAs were performed using Abnova ELISA kit KA1877.
614
615 **Imaging and quantification**
616 Imaging was performed on a Zeiss Axio Scan.Z1 automated slide scanner, Leica M165 FC equipped with
617 Leica DFC310 FX camera, and a Nikon Eclipse Ni microscope with a DS-Ri2 camera. Quantification of all
618 images was conducted blindly. For imaging of intact contralateral limbs, representative sections
619 displaying all tissue types (bone and cartilage, soft internal tissues, and epidermis) were selected. For the
620 tissue type analysis of EdU+ nuclei, tissues were classified as epidermis, “skeletal elements” (bone,
621 cartilage), and “soft tissues” (muscle, joint, tendon, ligaments, dermis, vasculature, and nerves) based on
622 nuclear morphology and location as previously described (Whited et al, 2013). All cell counts were
623 conducted utilizing CellProfiler.[61] Measurements of blastema area were performed using Fiji.[62] For *Prrx1*
624 HCR signal quantifications, the wound epidermis was first masked from each image. *Prrx1* fluorescence
625 intensity was normalized to the area of the blastema as measured by the DAPI signal.
626
627
628 **Cell dissociation, FACS isolation, and single-cell RNA-sequencing**
629 To isolate single cells, 12-16 homeostatic or systemically-activated limbs at 14 days post-amputation
630 were pooled for each biological replicate and dissociated in 4 ml of dissociation buffer (100 mg/ml
631 liberase diluted in 0.7X PBS with 0.5 U/ml DNase I) for 30 min at room temperature with gentle mixing.
632 Suspensions were filtered through 70 mm strainers to remove cell clumps and debris, and strainers were
633 washed with 1 ml of 0.7X PBS. Cells were spun down at 300 g at room temperature and resuspended in
634 1 ml of 0.7X PBS-0.04% BSA. Cells were then stained with 1 mg/ml Hoecsht, calcein AM, and propidium
635 iodide for isolation of alive, dividing (4C) and non-dividing (2C) cells by fluorescence activated cell sorting.
636 The purified cells were then sequenced at the Bauer Core Facility at Harvard University using an Illumina
637 NovaSeq 6000 [https://www.illumina.com]. Paired end reads were demultiplexed with bcl2fastq2 (V2.2.1)
638 (RRRID:SCR_015058).

ATAC-seq Library Prep and Sequencing

Ten thousand sorted 4C cells from homeostatic, systemically-activated, and regenerating limbs were resuspended in 5 µL PBS. 42.5 µL of transposition buffer (38.8mM tris-acetate, 77.6mM potassium acetate, 11.8mM magnesium acetate, 0.12% NP-40, 18.8% DMF, 0.47% protease inhibitor cocktail) was added to the cells, mixed, and incubated 10 min at room temperature. 2.5 µL of pre-loaded Tn5 (Diagenode cat# C01070012) was added to the reaction mixture. The transposition reaction was carried out at 37°C for 30 min with shaking at 300 rpm. Following transposition, the samples were purified through Direct-zol RNA MiniPrep kit (Zymo Research cat# R2050). Purified library fragments were amplified with custom primers 1 and 2 using the following conditions: 72°C for 5min; 98°C for 30s; and thermocycling at 98°C for 10s, 72°C for 30s and 72°C for 1min. The libraries were amplified for five cycles. Soon after, 5µL aliquot of the PCR reaction was added with 10µL of the PCR cocktail with SYBR Green (0.6Xfinal concentration). 20 cycles of PCR was performed to determine the additional number of cycles needed for the remaining 45 µL reaction. The libraries were purified using Direct-zol RNA MiniPrep kit. Purified libraries were sequenced at The Bauer Core Facility at Harvard University using an Illumina NovaSeq 6000 [https://www.illumina.com]. Paired End reads were demultiplexed with bcl2fastq2 (V2.2.1) (RRID: SCR_015058).

Bulk RNA isolation, sequencing, and computational analyses

βIIItub:GAP43-EGFP transgenic animals were used for RNA sequencing experiments to allow for easily identifiable collections of tissues.[56] RNA was extracted from tissue samples with Trizol (15596018, Ambion) and chloroform (288306, Sigma Aldrich). RNA was then isolated from tissue samples using a Zymo Clean Up and Concentrator kit (R1013). RNA samples were processed at the Bauer Core Facility at Harvard University using the Illumina NextSeq 500. Paired End reads were demultiplexed with bcl2fastq2 v2.2.

QUANTIFICATION AND STATISTICAL ANALYSIS

Minigenome

A custom reference "minigenome" was created by first performing in silico normalization on the sequenced reads by sample with Trinity (V2.12.0)[63] with the following parameters: --CPU 10 --max_memory 50G --no_run_inchworm --min_kmer_cov 2 --trimmomatic --seqType fq, before assembling them with parameters: --CPU 10 --max_memory 50G --min_kmer_cov 3 --seqType fa --no_normalize_reads. This transcriptome was then aligned to the entire axolotl genome (V6.0.0) [https://www.axolotl-omics.org/assemblies][64] using minimap2 (V2.24)][65] and the parameters -ax splice --secondary=no -O6,24 -B4 -L -t 20 -cs -ub -G 100000 to create genome intervals of the genes present in the transcriptome. The intervals were converted from the original SAMtools (V1.15.1)[66] format to BED using BEDOPS (V2.4.25).[67] Finally, the minigenome and annotation was created from the intervals using ShrinkGenome [https://github.com/brianjohnhaas/ShrinkGenome]. The complete axolotl mitochondrial genome [https://www.ncbi.nlm.nih.gov/nuccore/NC_005797][68] was then appended to this minigenome. We prevented competitive alignments to mitochondrial contributors downstream by masking their genomic loci using the maskFastaFromBed function from BEDTools (V2.30.0).[69]

Single-cell RNA-sequencing read quantification

We used Kallisto (V0.48.0)[70] to create an index, as well as pseudoalign the RNA-seq data before creating BUS [71] files by biological replicante. The BUS files were sorted and converted into text using bustools (V0.41.0)[72] using default parameters before converting the BUS files into sparse matrices of gene by cell data in R using BUSpaRse (V1.9.0).[73] The gene by cell sparse matrices were converted into Seurat[74] objects in R, filtering out cells with less than 200 transcripts as well as any feature that was in less than 3

cells, before merging the sample replicates into either homeostatic samples or systemically activated samples, which were merged into a single data structure, while maintaining their original metadata. For QC, cells were scored for their complexity with the following formula cell complexity = $\log_{10}$(# of genes in cell) / $\log_{10}$(# of UMI in cell). If a cell had less than 1,000 UMI while also both expressing less than 350 features and a cell complexity score less than 0.75 it was not considered a candidate for analysis and removed from the dataset.

Cell clustering and visualization

Clustering the cells was performed with Seurat (V4.1.0). Default parameters were used in the FindVariableFeatures function of Seurat to determine the number of principal components. We used a resolution of 1.0 to cluster the cells with 17 dimensions. We generated markers for the clusters and found that one of the clusters consisted primarily of mitochondrial markers. This cluster was eliminated and the cell clustering pipeline was repeated. We performed homotypic doublet proportion estimation to predict and remove doublets using DoubletFinder (V2.0.3)[74] as described at [https://github.com/chris-mcginnis-ucsf/DoubletFinder]. The cell clusters were visualized with the reduction method UMAP. Clusters were identified by unique markers in each cluster.

Differential gene expression analysis for single-cell RNA sequencing

We searched for differentially expressed genes between the homeostatic and systemically activated cells using DESeq2 (V1.36.0).[75] The contrast in the results was configured by condition, where homeostatic limb was the baseline and systemically activated limb was the contrasting condition. The results were determined to be significant if the adjusted p value was less than 0.1. Statistically significant results were visualized with ggplot2 (V3.3.6).[76]

CellChat analysis

To obtain the information related to incoming and outgoing clusters ligand-receptors interactions, we used the CellChat package[77] for 4C datasets using the previously generated Seurat objects. A custom axolotl ligand-receptor reference was generated using the minigenome. The database included information on ligands and receptors, and for orthologous gene repeats that have different positions in the genome and different annotations, labeled as “Gene_ik”, where k is the number of the repeats. The database was reconstructed following the ligand-receptor pairs used for the mouse CellChat database with the gene repeats included as separated ligand-receptor pairs (L1-R1, L1_i1_R1, etc.).
After generating the database, we followed the standard CellChat pipeline [https://github.com/sqjin/CellChat/]. To avoid the projection reducing the dropout effects of signaling genes, for possible zero expression of subunits of ligands/receptors, we used raw.use = FALSE setting in computeCommunProb function. We also used population.size = TRUE parameter to consider the effect of cell proportion in each cell group in the probability calculation. The chord diagrams were generated using netVisual_aggregate() function.

RNA Velocity

Upon the clusters to states annotation, we utilized Cell ranger, samtools, velocyto, and scvelo packages to perform the RNA Velocity analysis[78]. For the previously generated Cellranger output folder, we used the samtools sort function in the samtools package (-t CB -O BAM) to create the cellsorted_possorted_genome_bam.bam file from the possorted_genome_bam.bam file. The generated file was used for making the .loom file upon utilizing the velocyto run10x function of the velocyto package, using the minigenome. We tgeb converted the .h5Seurat annotated objects to .h5ad objects to transfer them from R to the Python environment. We used the scvelo package[79] for the RNA Velocity analysis. We merged .loom files with the respective data files previously generated, processed, and annotated. The following files were filtered and normalized. The first and second order moments (means and uncentered

variances) were computed among nearest neighbors in PCA space with the scvelo.pp.moments() function. Then we estimated velocity (scvelo.tl.velocity()), built the velocity_graph (scvelo.tl.velocity_graph()) and projected the velocities using scvelo.pl.velocity_embedding_stream() and scvelo.pl.velocity_embedding_grid() on UMAP (basis = 'umap') embedding. With that, we quantified pseudotime, latent time, and built the latent-time-based heatmaps with gene RNA abundance analysis.

Bulk RNA-seq dataset processing

The reads were trimmed for quality and adapters with Trimmomatic v0.39[80] with the following parameters: LEADING:3 TRAILING:3 SLIDINGWINDOW:4:15 MINLEN:36. An index of the previously published axolotl transcriptome[5] was created using Kallisto v0.45.1[70]. Sequence based bias correction was performed using Kallisto with 200 bootstraps across 20 threads. The transcript-level abundances from Kallisto were summarized and imported into R as a matrix of counts using tximport v1.0.3[81].

Differentially expressed genes were determined by estimating fold change and dispersion using DESeq2[75]. Genes were considered significant if they had a logarithmic fold change greater than 1.5 and adjusted p value of 5%. These significant genes were visualized using pheatmap v1.0.12.[82] Pathway analysis was performed in R using pathfinder.[83]

Chunked Genome

A custom "chunked genome" was needed for compatibility with tools used to process the alignments. We broke the large chromosomes of the axolotl genome (V6.0.0) [https://www.axolotl-omics.org/assemblies][68] into chunks smaller than 500M using ChunkGenome [https://github.com/brianjohnhaas/ChunkGenome]. ChunkGenome was also used to create a new feature coordinates from the original GTF. The complete axolotl mitochondrial genome [https://www.ncbi.nlm.nih.gov/nuccore/NC_005797][68] was appended to this chunked genome. We prevented competitive alignments to mitochondrial contributors downstream by masking their genomic loci using the maskFastaFromBed function from BEDTools (V2.30.0) [https://github.com/arq5x/bedtools2].[69]

Read processing for ATAC-seq

The sequencing data was aligned to the reference using Bowtie2 (V2.3.2)[84] using the parameters '--no-mixed -X 2000 --dovetail --no-discordant'. Samtools (V1.10)[85] was used to keep the alignments sorted and indexed throughout the processing. We removed all alignments to mitochondria by simply using the grep -v chrM before filtering out the low quality alignments using Samtools view -q 30. The Picard Toolkit [https://broadinstitute.github.io/picard/] was used to remove PCR and optical duplicates using Picard's MarkDuplicates with the parameters 'ASSUME_SORTED=true REMOVE_DUPLICATES=true SORTING_COLLECTION_SIZE_RATIO=0.2'. Coverage tracks of the alignments were generated with deepTools[86] bamCoverage with parameters '--outFileFormat=bigwig --normalizeUsing CPM -p 16 --binSize 20'.

ATAC-seq Peak Calling

Sites of genomic enrichment were found using Genrich (V0.5) (https://github.com/jsh58/Genrich#atacseq) in ATAC-seq mode using default arguments '-j -q 0.05', the results of which were converted to bigwig format using bedGraphToBigWig[87]. We evaluated the consistency of the Genrich generated peaks using Irreproducible Discovery Rate (IDR) (V2.0.4.2)[88]. We filtered these conservative peaks even further as described in the guidelines and practices of the ENCODE consortia[88]. We counted these peaks with high rank consistency by first extending the coordinates of the peaks with bedtools (V2.30.0)[69] function slop with argument '-b 500' before merging all the pooled replicates with bedtools merge, then finally using the intersect function with parameters '-wo'.

Annotating and visualizing the ATAC data

We used ChIPseeker (V1.32.1)[89] to annotate the peaks. The counts were put together into a genes by peak count matrix and differential expression was observed using DESeq2[75]. Pheatmap (V1.9.12)[82] was used to visualize the normalized counts. We clustered the samples based on their similarity using pcaExplorer (V2.22.0)[90]. Genome browser tracks of all the peaks were plotted against the total coverage of all of the reads using pyGenomeTracks (V3.8).[91]

SUPPLEMENTAL FIGURE LEGENDS

Figure S1. Marker genes used to identify clusters in single-cell RNA sequencing of 4C and 2C cells (Related to Figure 2)
(A) Dot plots showing the relative frequency of expression (dot size) and expression level (color) for marker genes across all clusters of 4C cells. **(B)** Latent time-ordered heatmaps demonstrating variable genes across 4C fibroblast clusters. **(C)** Gene dynamics analysis shows the top 15 genes across the 4C cells with the most unique RNA abundance portraits. X-axis shows the spliced and the y-axis shows the unspliced transcripts for the gene, the steady state marked with the line. Each dot represents a single cell, with colors describing the clusters indicated on the right. **(D)** Dot plots showing the relative frequency of expression (dot size) and expression level (color) for marker genes across all clusters of 4C cells.

Figure S2. Inhibition of mTOR signaling with rapamycin delays regeneration (Related to Figure 3)
(A) Regenerating limbs at 7 dpa treated with rapamycin or vehicle control. Arrowheads mark the amputation plane. **(B)** Blastema growth curves of rapamycin or vehicle treated animals (n = 10 animals per group). Statistical significance was determined using unpaired two-tailed Welch's t-test with Holm-Šídák correction). **(C)** Representative skeletal preparations of regenerated limbs with Alcian blue and Alizarin red at 10 weeks post-amputation. Scale bars, 0.5 mm.

Figure S3. Adrenergic receptors expression in proliferating fibroblasts (Related to Figure 5) (Related to Figure 4)
Dot plot showing the relative frequency of expression (dot size) and expression level (color) for adrenergic receptors across all clusters of 4C cells.

Figure S4. Effects of inhibiting Wnt and Igf1r signaling on systemic activation (Related to Figure 4)
(A-B) Chord diagrams of CellChat analysis of Igf1r signaling **(A)** and insulin signaling **(B)** between 4C cell types identified by scRNA-seq in Figure 2. **(C)** EdU and DAPI staining of limbs contralateral to unilateral amputations treated with tankyrase inhibitor IWR-1, Igf1r inhibitor NVP-ADW742 or vehicle control, harvested at 7 days post amputation. **(D)** Quantification of percent EdU positive nuclei of contralateral limbs in (A) (n = 11 animals for vehicle control, n = 14 animals for IWR-1 and NVP-ADW742). All data shown as mean ± SD. Statistical significance was determined using Welch's ANOVA with Dunnett's T3 correction, W = 4.883. Scale bar, 500 μm. NVP, NVP-ADW742. EdU, 5-ethynyl-2′-deoxyuridine.

SUPPLEMENTAL EXCEL TABLE LEGENDS

Table S1. List of transcripts expressed by each cluster of 4C cells in homeostatic and systemically-activated limbs (Related to Figure 2).

838 **Table S2.** Differentially expressed transcripts expressed by each cluster of 4C cells in homeostatic and
839 systemically-activated limbs (Related to Figure 2).
840
841 **Table S3.** List of transcripts expressed by each cluster of 2C cells in homeostatic and systemically-
842 activated limbs (Related to Figure 2).
843
844 **Table S4.** Differentially expressed transcripts expressed by each cluster of 2C cells in homeostatic and
845 systemically-activated limbs (Related to Figure 2).
846
847 **Table S5.** List of differentially expressed transcripts between sham-operated and denervated forelimbs
848 contralateral to unilateral amputations (Related to Figure 4).
849
850 **Table S6.** List of abundant peaks identified across 4C cells of homeostatic, activated, and regenerating
851 limbs and differentially abundant peaks across pairwise comparisons. (Related to Figure 6).
852
853
854

References

1. Spallanzani, L. (1769 [Italian: 1768].). Reproductions of the legs in the aquatic salamander. In An Essay on Animal Reproductions [Prodromo di un opera da imprimersi sopra la riproduzioni anamali], (Becket and de Hondt), pp. 68-72.
2. Simon, A., and Tanaka, E.M. (2013). Limb regeneration. Wiley Interdiscip Rev Dev Biol *2*, 291-300. 10.1002/wdev.73.
3. Voss, S.R., Palumbo, A., Nagarajan, R., Gardiner, D.M., Muneoka, K., Stromberg, A.J., and Athippozhy, A.T. (2015). Gene expression during the first 28 days of axolotl limb regeneration I: Experimental design and global analysis of gene expression. Regeneration (Oxford, England) *2*, 120-136. 10.1002/reg2.37.
4. Stewart, R., Rascon, C.A., Tian, S., Nie, J., Barry, C., Chu, L.F., Ardalani, H., Wagner, R.J., Probasco, M.D., Bolin, J.M., et al. (2013). Comparative RNA-seq analysis in the unsequenced axolotl: the oncogene burst highlights early gene expression in the blastema. PLoS computational biology *9*, e1002936. 10.1371/journal.pcbi.1002936.
5. Bryant, D.M., Johnson, K., DiTommaso, T., Tickle, T., Couger, M.B., Payzin-Dogru, D., Lee, T.J., Leigh, N.D., Kuo, T.H., Davis, F.G., et al. (2017). A Tissue-Mapped Axolotl De Novo Transcriptome Enables Identification of Limb Regeneration Factors. Cell reports *18*, 762-776. 10.1016/j.celrep.2016.12.063.
6. Gerber, T., Murawala, P., Knapp, D., Masselink, W., Schuez, M., Hermann, S., Gac-Santel, M., Nowoshilow, S., Kageyama, J., Khattak, S., et al. (2018). Single-cell analysis uncovers convergence of cell identities during axolotl limb regeneration. Science *362*. 10.1126/science.aaq0681.
7. Leigh, N.D., Dunlap, G.S., Johnson, K., Mariano, R., Oshiro, R., Wong, A.Y., Bryant, D.M., Miller, B.M., Ratner, A., Chen, A., et al. (2018). Transcriptomic landscape of the blastema niche in regenerating adult axolotl limbs at single-cell resolution. Nat Commun *9*, 5153. 10.1038/s41467-018-07604-0.
8. Ricci, L., and Srivastava, M. (2018). Wound-induced cell proliferation during animal regeneration. Wiley Interdiscip Rev Dev Biol *7*, e321. 10.1002/wdev.321.
9. Wenemoser, D., and Reddien, P.W. (2010). Planarian regeneration involves distinct stem cell responses to wounds and tissue absence. Developmental biology *344*, 979-991. 10.1016/j.ydbio.2010.06.017.
10. Newmark, P.A., and Sanchez Alvarado, A. (2000). Bromodeoxyuridine specifically labels the regenerative stem cells of planarians. Dev Biol *220*, 142-153. 10.1006/dbio.2000.9645.
11. Salo, E., and Baguna, J. (1984). Regeneration and pattern formation in planarians. I. The pattern of mitosis in anterior and posterior regeneration in Dugesia (G) tigrina, and a new proposal for blastema formation. J Embryol Exp Morphol *83*, 63-80.
12. Johnson, K., Bateman, J., DiTommaso, T., Wong, A.Y., and Whited, J.L. (2018). Systemic cell cycle activation is induced following complex tissue injury in axolotl. Developmental biology *433*, 461-472. 10.1016/j.ydbio.2017.07.010.
13. Satoh, A., Gardiner, D.M., Bryant, S.V., and Endo, T. (2007). Nerve-induced ectopic limb blastemas in the Axolotl are equivalent to amputation-induced blastemas. Dev Biol *312*, 231-244. 10.1016/j.ydbio.2007.09.021.
14. Dumont, N.A., Bentzinger, C.F., Sincennes, M.C., and Rudnicki, M.A. (2015). Satellite Cells and Skeletal Muscle Regeneration. Compr Physiol *5*, 1027-1059. 10.1002/cphy.c140068.
15. Muneoka, K., Holler-Dinsmore, G.V., and Bryant, S.V. (1985). A quantitative analysis of regeneration from chimaeric limb stumps in the axolotl. J Embryol Exp Morphol *90*, 1-12.
16. Muneoka, K., Fox, W.F., and Bryant, S.V. (1986). Cellular contribution from dermis and cartilage to the regenerating limb blastema in axolotls. Dev Biol *116*, 256-260.
17. Kragl, M., Knapp, D., Nacu, E., Khattak, S., Maden, M., Epperlein, H.H., and Tanaka, E.M. (2009). Cells keep a memory of their tissue origin during axolotl limb regeneration. Nature *460*, 60-65. nature08152 [pii]
10.1038/nature08152.
18. McCusker, C.D., Diaz-Castillo, C., Sosnik, J., A, Q.P., and Gardiner, D.M. (2016). Cartilage and bone cells do not participate in skeletal regeneration in Ambystoma mexicanum limbs. Developmental biology *416*, 26-33. 10.1016/j.ydbio.2016.05.032.

19. Carver, E.A., Jiang, R., Lan, Y., Oram, K.F., and Gridley, T. (2001). The mouse snail gene encodes a key regulator of the epithelial-mesenchymal transition. Mol Cell Biol *21*, 8184-8188. 10.1128/MCB.21.23.8184-8188.2001.
20. Barbera, M.J., Puig, I., Dominguez, D., Julien-Grille, S., Guaita-Esteruelas, S., Peiro, S., Baulida, J., Franci, C., Dedhar, S., Larue, L., and Garcia de Herreros, A. (2004). Regulation of Snail transcription during epithelial to mesenchymal transition of tumor cells. Oncogene *23*, 7345-7354. 10.1038/sj.onc.1207990.
21. Lamouille, S., Xu, J., and Derynck, R. (2014). Molecular mechanisms of epithelial-mesenchymal transition. Nat Rev Mol Cell Biol *15*, 178-196. 10.1038/nrm3758.
22. Buckbinder, L., Talbott, R., Seizinger, B.R., and Kley, N. (1994). Gene regulation by temperature-sensitive p53 mutants: identification of p53 response genes. Proc Natl Acad Sci U S A *91*, 10640-10644. 10.1073/pnas.91.22.10640.
23. Haidurov, A., and Budanov, A.V. (2020). Sestrin family - the stem controlling healthy ageing. Mech Ageing Dev *192*, 111379. 10.1016/j.mad.2020.111379.
24. La Manno, G., Soldatov, R., Zeisel, A., Braun, E., Hochgerner, H., Petukhov, V., Lidschreiber, K., Kastriti, M.E., Lonnerberg, P., Furlan, A., et al. (2018). RNA velocity of single cells. Nature *560*, 494-498. 10.1038/s41586-018-0414-6.
25. Rodgers, J.T., King, K.Y., Brett, J.O., Cromie, M.J., Charville, G.W., Maguire, K.K., Brunson, C., Mastey, N., Liu, L., Tsai, C.R., et al. (2014). mTORC1 controls the adaptive transition of quiescent stem cells from G0 to G(Alert). Nature *510*, 393-396. 10.1038/nature13255.
26. Rodgers, J.T., Schroeder, M.D., Ma, C., and Rando, T.A. (2017). HGFA Is an Injury-Regulated Systemic Factor that Induces the Transition of Stem Cells into GAlert. Cell reports *19*, 479-486. 10.1016/j.celrep.2017.03.066.
27. Jin, S., Guerrero-Juarez, C.F., Zhang, L., Chang, I., Ramos, R., Kuan, C.H., Myung, P., Plikus, M.V., and Nie, Q. (2021). Inference and analysis of cell-cell communication using CellChat. Nat Commun *12*, 1088. 10.1038/s41467-021-21246-9.
28. Takeuchi, K., Shibamoto, S., Nagamine, K., Shigemori, I., Omura, S., Kitamura, N., and Ito, F. (2001). Signaling pathways leading to transcription and translation cooperatively regulate the transient increase in expression of c-Fos protein. J Biol Chem *276*, 26077-26083. 10.1074/jbc.M102704200.
29. Brown, E.J., Albers, M.W., Shin, T.B., Ichikawa, K., Keith, C.T., Lane, W.S., and Schreiber, S.L. (1994). A mammalian protein targeted by G1-arresting rapamycin-receptor complex. Nature *369*, 756-758. 10.1038/369756a0.
30. Renthal, W., Tochitsky, I., Yang, L., Cheng, Y.C., Li, E., Kawaguchi, R., Geschwind, D.H., and Woolf, C.J. (2020). Transcriptional Reprogramming of Distinct Peripheral Sensory Neuron Subtypes after Axonal Injury. Neuron *108*, 128-144 e129. 10.1016/j.neuron.2020.07.026.
31. Rao, Y. (2019). The First Hormone: Adrenaline. Trends Endocrinol Metab *30*, 331-334. 10.1016/j.tem.2019.03.005.
32. Jabir, N.R., Firoz, C.K., Zughaibi, T.A., Alsaadi, M.A., Abuzenadah, A.M., Al-Asmari, A.I., Alsaieedi, A., Ahmed, B.A., Ramu, A.K., and Tabrez, S. (2022). A literature perspective on the pharmacological applications of yohimbine. Ann Med *54*, 2861-2875. 10.1080/07853890.2022.2131330.
33. Tam, S.W., Worcel, M., and Wyllie, M. (2001). Yohimbine: a clinical review. Pharmacol Ther *91*, 215-243. 10.1016/s0163-7258(01)00156-5.
34. Black, J.W., Crowther, A.F., Shanks, R.G., Smith, L.H., and Dornhorst, A.C. (1964). A New Adrenergic Betareceptor Antagonist. Lancet *1*, 1080-1081. 10.1016/s0140-6736(64)91275-9.
35. Mitsiades, C.S., Mitsiades, N.S., McMullan, C.J., Poulaki, V., Shringarpure, R., Akiyama, M., Hideshima, T., Chauhan, D., Joseph, M., Libermann, T.A., et al. (2004). Inhibition of the insulin-like growth factor receptor-1 tyrosine kinase activity as a therapeutic strategy for multiple myeloma, other hematologic malignancies, and solid tumors. Cancer Cell *5*, 221-230. 10.1016/s1535-6108(04)00050-9.
36. Kawakami, Y., Rodriguez Esteban, C., Raya, M., Kawakami, H., Marti, M., Dubova, I., and Izpisua Belmonte, J.C. (2006). Wnt/beta-catenin signaling regulates vertebrate limb regeneration. Genes & development *20*, 3232-3237. 10.1101/gad.1475106.

37. Aztekin, C., Hiscock, T.W., Marioni, J.C., Gurdon, J.B., Simons, B.D., and Jullien, J. (2019). Identification of a regeneration-organizing cell in the Xenopus tail. Science *364*, 653-658. 10.1126/science.aav9996.
38. Srivastava, M., Mazza-Curll, K.L., van Wolfswinkel, J.C., and Reddien, P.W. (2014). Whole-body acoel regeneration is controlled by Wnt and Bmp-Admp signaling. Current biology : CB *24*, 1107-1113. 10.1016/j.cub.2014.03.042.
39. Lander, R., and Petersen, C.P. (2016). Wnt, Ptk7, and FGFRL expression gradients control trunk positional identity in planarian regeneration. Elife *5*. 10.7554/eLife.12850.
40. Petersen, C.P., and Reddien, P.W. (2009). A wound-induced Wnt expression program controls planarian regeneration polarity. Proc Natl Acad Sci U S A *106*, 17061-17066. 10.1073/pnas.0906823106.
41. Chen, B., Dodge, M.E., Tang, W., Lu, J., Ma, Z., Fan, C.W., Wei, S., Hao, W., Kilgore, J., Williams, N.S., et al. (2009). Small molecule-mediated disruption of Wnt-dependent signaling in tissue regeneration and cancer. Nat Chem Biol *5*, 100-107. 10.1038/nchembio.137.
42. Taira, N., Mimoto, R., Kurata, M., Yamaguchi, T., Kitagawa, M., Miki, Y., and Yoshida, K. (2012). DYRK2 priming phosphorylation of c-Jun and c-Myc modulates cell cycle progression in human cancer cells. The Journal of Clinical Investigation *122*, 859-872. 10.1172/jci60818.
43. Todd, J.T. (1823). On the process of reproduction of the members of the aquatic salamander. . The Quarterly Journal of Science, Literature, and the Arts. *16*, 84-96.
44. Singer, M. (1946). The nervous system and regeneration of the forelimb of adult Triturus; the influence of number of nerve fibers, including a quantitative study of limb innervation. J Exp Zool *101*, 299-337.
45. Singer, M. (1952). The influence of the nerve in regeneration of the amphibian extremity. Q Rev Biol *27*, 169-200.
46. Brockes, J.P. (1987). The nerve dependence of amphibian limb regeneration. The Journal of experimental biology *132*, 79-91.
47. Farkas, J.E., and Monaghan, J.R. (2017). A brief history of the study of nerve dependent regeneration. Neurogenesis (Austin) *4*, e1302216. 10.1080/23262133.2017.1302216.
48. Wells, K.M., Kelley, K., Baumel, M., Vieira, W.A., and McCusker, C.D. (2021). Neural control of growth and size in the axolotl limb regenerate. Elife *10*. 10.7554/eLife.68584.
49. Tassava, R.A., and Loyd, R.M. (1977). Injury requirement for initiation of regeneration of newt limbs which have whole skin grafts. Nature *268*, 49-50. 10.1038/268049a0.
50. Zeng, A., Li, H., Guo, L., Gao, X., McKinney, S., Wang, Y., Yu, Z., Park, J., Semerad, C., Ross, E., et al. (2018). Prospectively Isolated Tetraspanin(+) Neoblasts Are Adult Pluripotent Stem Cells Underlying Planaria Regeneration. Cell *173*, 1593-1608 e1520. 10.1016/j.cell.2018.05.006.
51. Zhang, X., Yalcin, S., Lee, D.F., Yeh, T.Y., Lee, S.M., Su, J., Mungamuri, S.K., Rimmele, P., Kennedy, M., Sellers, R., et al. (2011). FOXO1 is an essential regulator of pluripotency in human embryonic stem cells. Nat Cell Biol *13*, 1092-1099. 10.1038/ncb2293.
52. Ogg, S., Paradis, S., Gottlieb, S., Patterson, G.I., Lee, L., Tissenbaum, H.A., and Ruvkun, G. (1997). The Fork head transcription factor DAF-16 transduces insulin-like metabolic and longevity signals in C. elegans. Nature *389*, 994-999. 10.1038/40194.
53. Brunet, A., Bonni, A., Zigmond, M.J., Lin, M.Z., Juo, P., Hu, L.S., Anderson, M.J., Arden, K.C., Blenis, J., and Greenberg, M.E. (1999). Akt promotes cell survival by phosphorylating and inhibiting a Forkhead transcription factor. Cell *96*, 857-868. 10.1016/s0092-8674(00)80595-4.
54. Collins, J.P., Cheek, J.E. (1983). Effect of Food and Density on Development of Typical and Cannibalistic Salamander Larvae in Ambystoma tigrinum nebulosum. Integr Comp Biol *23*, 77-84.
55. Keel, M., and Trentz, O. (2005). Pathophysiology of polytrauma. Injury *36*, 691-709. 10.1016/j.injury.2004.12.037.
56. Khattak, S., Schuez, M., Richter, T., Knapp, D., Haigo, S.L., Sandoval-Guzman, T., Hradlikova, K., Duemmler, A., Kerney, R., and Tanaka, E.M. (2013). Germline transgenic methods for tracking cells and testing gene function during regeneration in the axolotl. Stem cell reports *1*, 90-103. 10.1016/j.stemcr.2013.03.002.
57. Schotté, O.E., and Butler, E.G. (1941). Morphological effects of denervation and amputation of limbs in urodele larvae. Journal of Experimental Zoology *87*, 279-322. https://doi.org/10.1002/jez.1400870207.

58. Kropf, N., Krishnan, K., Chao, M., Schweitzer, M., Rosenberg, Z., and Russell, S.M. (2010). Sciatic nerve injury model in the axolotl: functional, electrophysiological, and radiographic outcomes. J Neurosurg *112*, 880-889. 10.3171/2008.10.Jns08222.
59. Lovely, A.M., Duerr, T.J., Stein, D.F., Mun, E.T., and Monaghan, J.R. (2022). Hybridization Chain Reaction Fluorescence In Situ Hybridization (HCR-FISH) in Ambystoma mexicanum Tissue. In Salamanders: Methods and Protocols, (Springer), pp. 109-122.
60. Debuque, R.J., and Godwin, J.W. (2015). Methods for axolotl blood collection, intravenous injection, and efficient leukocyte isolation from peripheral blood and the regenerating limb. Methods Mol Biol *1290*, 205-226. 10.1007/978-1-4939-2495-0_17.
61. McQuin, C., Goodman, A., Chernyshev, V., Kamentsky, L., Cimini, B.A., Karhohs, K.W., Doan, M., Ding, L., Rafelski, S.M., Thirstrup, D., et al. (2018). CellProfiler 3.0: Next-generation image processing for biology. PLOS Biology *16*, e2005970. 10.1371/journal.pbio.2005970.
62. Schindelin, J., Arganda-Carreras, I., Frise, E., Kaynig, V., Longair, M., Pietzsch, T., Preibisch, S., Rueden, C., Saalfeld, S., Schmid, B., et al. (2012). Fiji: an open-source platform for biological-image analysis. Nature Methods *9*, 676-682. 10.1038/nmeth.2019.
63. Grabherr, M.G., Haas, B.J., Yassour, M., Levin, J.Z., Thompson, D.A., Amit, I., Adiconis, X., Fan, L., Raychowdhury, R., Zeng, Q., et al. (2011). Full-length transcriptome assembly from RNA-Seq data without a reference genome. Nat Biotechnol *29*, 644-652. 10.1038/nbt.1883.
64. Schloissnig, S., Kawaguchi, A., Nowoshilow, S., Falcon, F., Otsuki, L., Tardivo, P., Timoshevskaya, N., Keinath, M.C., Smith, J.J., Voss, S.R., and Tanaka, E.M. (2021). The giant axolotl genome uncovers the evolution, scaling, and transcriptional control of complex gene loci. Proceedings of the National Academy of Sciences of the United States of America *118*. 10.1073/pnas.2017176118.
65. Li, H. (2018). Minimap2: pairwise alignment for nucleotide sequences. Bioinformatics *34*, 3094-3100. 10.1093/bioinformatics/bty191.
66. Li, H., Handsaker, B., Wysoker, A., Fennell, T., Ruan, J., Homer, N., Marth, G., Abecasis, G., and Durbin, R. (2009). The Sequence Alignment/Map format and SAMtools. Bioinformatics *25*, 2078-2079. 10.1093/bioinformatics/btp352.
67. Neph, S., Kuehn, M.S., Reynolds, A.P., Haugen, E., Thurman, R.E., Johnson, A.K., Rynes, E., Maurano, M.T., Vierstra, J., Thomas, S., et al. (2012). BEDOPS: high-performance genomic feature operations. Bioinformatics *28*, 1919-1920. 10.1093/bioinformatics/bts277.
68. Arnason, U., Gullberg, A., Janke, A., Joss, J., and Elmerot, C. (2004). Mitogenomic analyses of deep gnathostome divergences: a fish is a fish. Gene *333*, 61-70. 10.1016/j.gene.2004.02.014.
69. Quinlan, A.R., and Hall, I.M. (2010). BEDTools: a flexible suite of utilities for comparing genomic features. Bioinformatics *26*, 841-842. 10.1093/bioinformatics/btq033.
70. Bray, N.L., Pimentel, H., Melsted, P., and Pachter, L. (2016). Near-optimal probabilistic RNA-seq quantification. Nat Biotechnol *34*, 525-527. 10.1038/nbt.3519.
71. Gao, F., da Veiga Beltrame, E., Gehring, J.A., Edljarn Hjoerleifsson, K.E., Lu, L., Melsted, P., Ntranos, V., Pachter, L., and Svensson, V. (2019). The BUS Format for Single-Cell RNA-Seq Processing and Analysis. J Biomol Tech *30*, S62-S62.
72. Melsted, P., Booeshaghi, A.S., Liu, L., Gao, F., Lu, L., Min, K.H.J., da Veiga Beltrame, E., Hjörleifsson, K.E., Gehring, J., and Pachter, L. (2021). Modular, efficient and constant-memory single-cell RNA-seq preprocessing. Nat Biotechnol *39*, 813-818. 10.1038/s41587-021-00870-2.
73. Moses L, P.L. (2022). BUSpaRse: kallisto | bustools R utilities.
74. Hao, Y., Hao, S., Andersen-Nissen, E., Mauck, W.M., 3rd, Zheng, S., Butler, A., Lee, M.J., Wilk, A.J., Darby, C., Zager, M., et al. (2021). Integrated analysis of multimodal single-cell data. Cell *184*, 3573-3587.e3529. 10.1016/j.cell.2021.04.048.
75. Love, M.I., Huber, W., and Anders, S. (2014). Moderated estimation of fold change and dispersion for RNA-seq data with DESeq2. Genome biology *15*, 550. 10.1186/s13059-014-0550-8.
76. Wickham, H. (2009). Elegant graphics for data analysis (ggplot2). Applied Spatial Data Analysis R.
77. Jin, S., Guerrero-Juarez, C.F., Zhang, L., Chang, I., Ramos, R., Kuan, C.-H., Myung, P., Plikus, M.V., and Nie, Q. (2021). Inference and analysis of cell-cell communication using CellChat. Nature communications *12*, 1088. 10.1038/s41467-021-21246-9.

78. La Manno, G., Soldatov, R., Zeisel, A., Braun, E., Hochgerner, H., Petukhov, V., Lidschreiber, K., Kastriti, M.E., Lönnerberg, P., Furlan, A., et al. (2018). RNA velocity of single cells. Nature *560*, 494-498. 10.1038/s41586-018-0414-6.
79. Bergen, V., Lange, M., Peidli, S., Wolf, F.A., and Theis, F.J. (2020). Generalizing RNA velocity to transient cell states through dynamical modeling. Nature Biotechnology *38*, 1408-1414. 10.1038/s41587-020-0591-3.
80. Bolger, A.M., Lohse, M., and Usadel, B. (2014). Trimmomatic: a flexible trimmer for Illumina sequence data. Bioinformatics *30*, 2114-2120. 10.1093/bioinformatics/btu170.
81. Soneson, C., Love, M.I., and Robinson, M.D. (2015). Differential analyses for RNA-seq: transcript-level estimates improve gene-level inferences. F1000Res *4*, 1521. 10.12688/f1000research.7563.2.
82. Kolde, R. (2019). pheatmap: Pretty Heatmaps. R package version 1.0. 12. R Packag. version 1.0 *8*.
83. Ulgen, E., Ozisik, O., and Sezerman, O.U. (2019). pathfindR: An R Package for Comprehensive Identification of Enriched Pathways in Omics Data Through Active Subnetworks. Front Genet *10*, 858. 10.3389/fgene.2019.00858.
84. Langmead, B., and Salzberg, S.L. (2012). Fast gapped-read alignment with Bowtie 2. Nat Methods *9*, 357-359. 10.1038/nmeth.1923.
85. Li, H., Handsaker, B., Wysoker, A., Fennell, T., Ruan, J., Homer, N., Marth, G., Abecasis, G., Durbin, R., and Subgroup, G.P.D.P. (2009). The Sequence Alignment/Map format and SAMtools. Bioinformatics *25*, 2078-2079. 10.1093/bioinformatics/btp352.
86. Ramírez, F., Ryan, D.P., Grüning, B., Bhardwaj, V., Kilpert, F., Richter, A.S., Heyne, S., Dündar, F., and Manke, T. (2016). deepTools2: a next generation web server for deep-sequencing data analysis. Nucleic acids research *44*, W160-165. 10.1093/nar/gkw257.
87. Kent, W.J., Zweig, A.S., Barber, G., Hinrichs, A.S., and Karolchik, D. (2010). BigWig and BigBed: enabling browsing of large distributed datasets. Bioinformatics *26*, 2204-2207. 10.1093/bioinformatics/btq351.
88. Li, Q., Brown, J.B., Huang, H., and Bickel, P.J. (2011). Measuring reproducibility of high-throughput experiments. The Annals of Applied Statistics *5*, 1752-1779, 1728.
89. Yu, G., Wang, L.-G., and He, Q.-Y. (2015). ChIPseeker: an R/Bioconductor package for ChIP peak annotation, comparison and visualization. Bioinformatics *31*, 2382-2383. 10.1093/bioinformatics/btv145.
90. Marini, F., and Binder, H. (2019). pcaExplorer: an R/Bioconductor package for interacting with RNA-seq principal components. BMC Bioinformatics *20*, 331. 10.1186/s12859-019-2879-1.
91. Lopez-Delisle, L., Rabbani, L., Wolff, J., Bhardwaj, V., Backofen, R., Grüning, B., Ramírez, F., and Manke, T. (2020). pyGenomeTracks: reproducible plots for multivariate genomic datasets Bioinformatics *37*, 422-423. 10.1093/bioinformatics/btaa692.
92. Carpenter, A.E., Jones, T.R., Lamprecht, M.R., Clarke, C., Kang, I.H., Friman, O., Guertin, D.A., Chang, J.H., Lindquist, R.A., Moffat, J., et al. (2006). CellProfiler: image analysis software for identifying and quantifying cell phenotypes. Genome biology *7*, R100. 10.1186/gb-2006-7-10-r100.
93. Bray, N.L., Pimentel, H., Melsted, P., and Pachter, L. (2016). Near-optimal probabilistic RNA-seq quantification. Nature Biotechnology *34*, 525-527. 10.1038/nbt.3519.

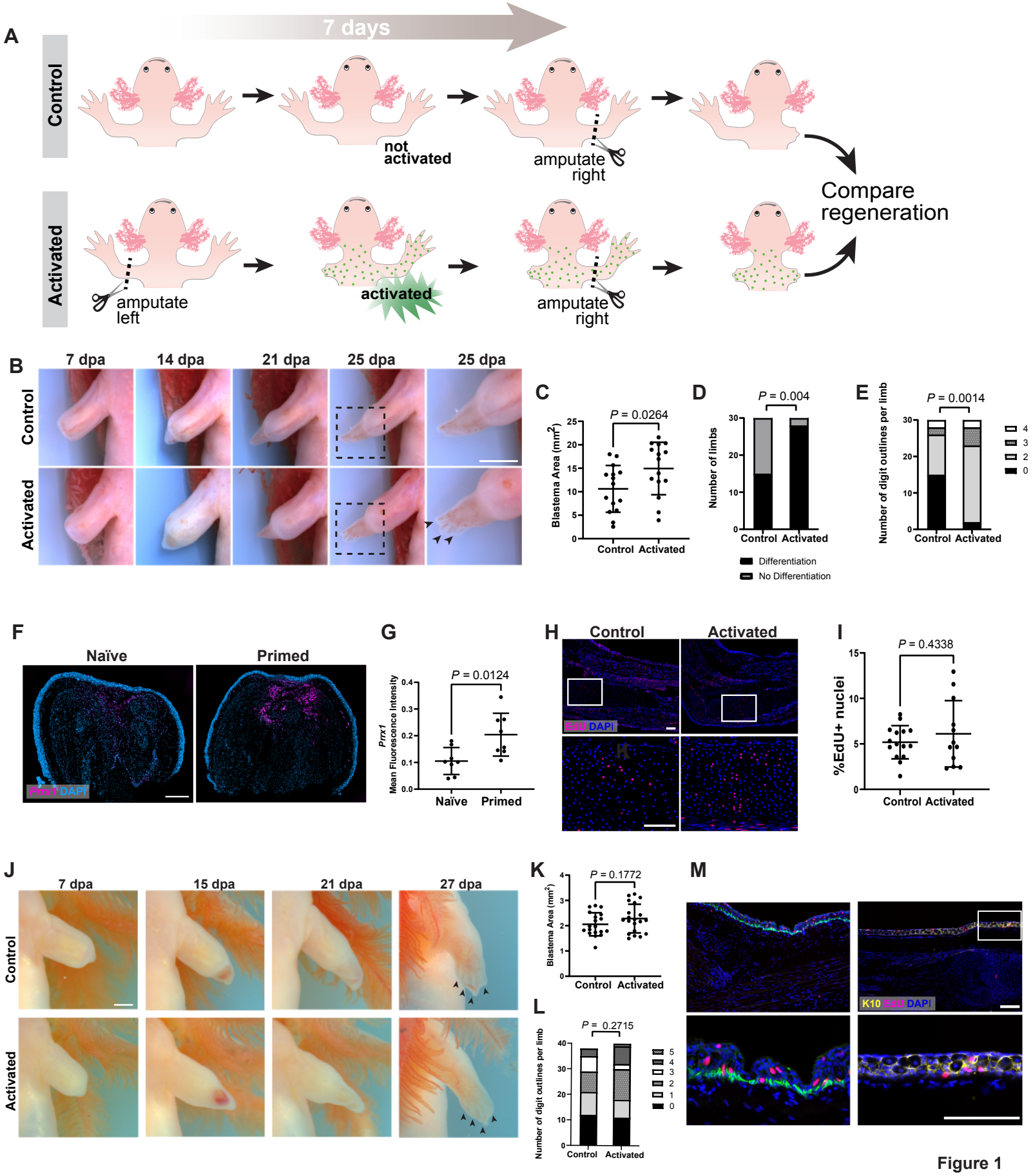
A
7 days
Control
not activated
amputate right
Activated
amputate left
activated
amputate right
Compare regeneration
B
7 dpa
14 dpa
21 dpa
25 dpa
25 dpa
Control
Activated
C
P = 0.0264
Blastema Area (mm2)
Control
Activated
D
P = 0.004
Number of limbs
Control
Activated
Differentiation
No Differentiation
E
P = 0.0014
Number of digit outlines per limb
Control
Activated
4
3
2
0
F
Naïve
Primed
Prrx1 DAPI
G
P = 0.0124
Prrx1 Mean Fluorescence Intensity
Naïve
Primed
H
Control
Activated
EdU DAPI
K
I
P = 0.4338
%EdU+ nuclei
Control
Activated
J
7 dpa
15 dpa
21 dpa
27 dpa
Control
Activated
K
P = 0.1772
Blastema Area (mm2)
Control
Activated
L
P = 0.2715
Number of digit outlines per limb
Control
Activated
5
4
3
2
1
0
M
K10 EdU DAPI

Figure 1

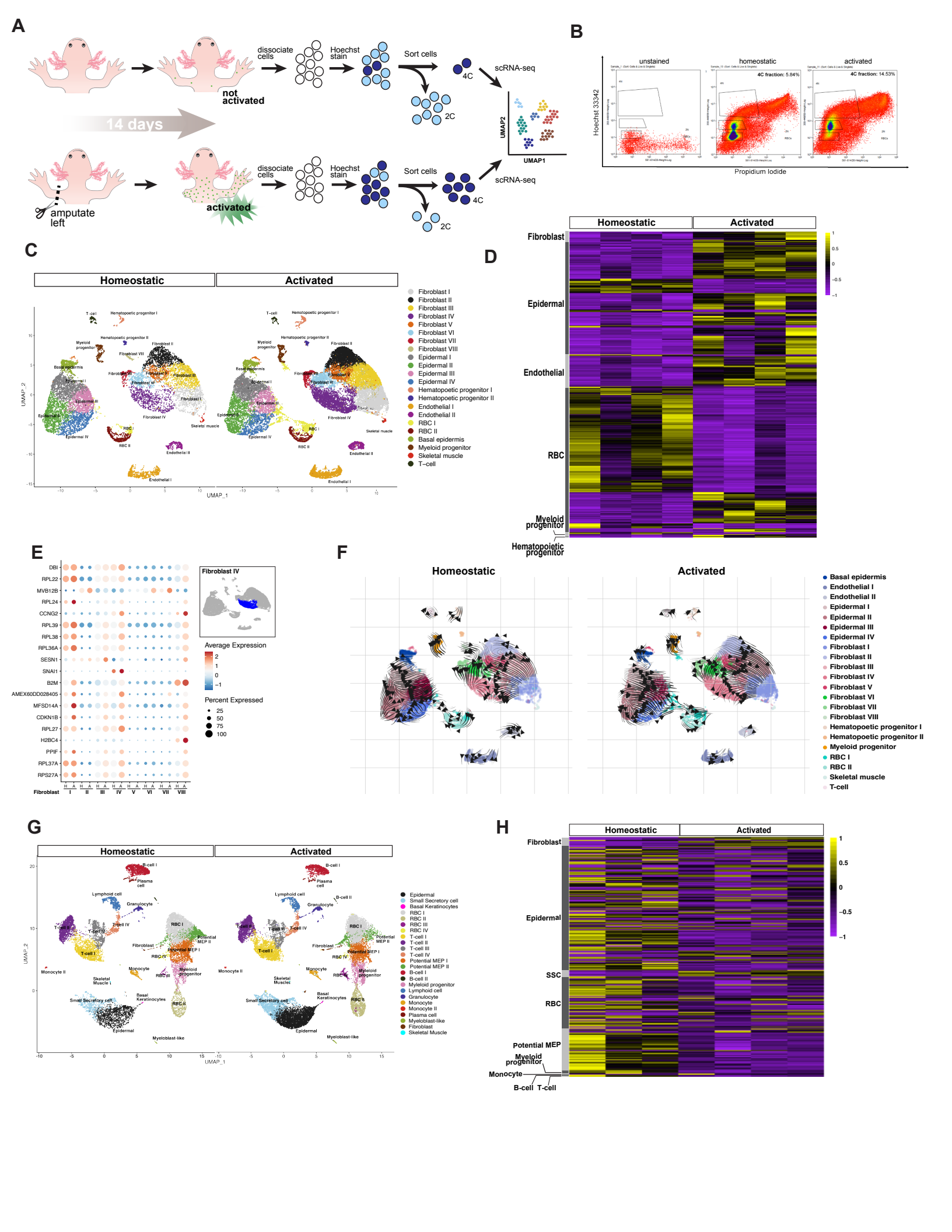
A
not activated
14 days
activated
amputate left
dissociate cells
Hoechst stain
Sort cells
4C
2C
scRNA-seq
UMAP2
UMAP1
B
unstained
homeostatic
activated
4C fraction: 5.84%
4C fraction: 14.53%
Hoechst 33342
Propidium Iodide
C
Homeostatic
Activated
UMAP_1
UMAP_2
Fibroblast I
Fibroblast II
Fibroblast III
Fibroblast IV
Fibroblast V
Fibroblast VI
Fibroblast VII
Fibroblast VIII
Epidermal I
Epidermal II
Epidermal III
Epidermal IV
Hematopoetic progenitor I
Hematopoetic progenitor II
Endothelial I
Endothelial II
RBC I
RBC II
Basal epidermis
Myeloid progenitor
Skeletal muscle
T–cell
D
Homeostatic
Activated
Fibroblast
Epidermal
Endothelial
RBC
Myeloid progenitor
Hematopoietic progenitor
E
Fibroblast IV
Average Expression
Percent Expressed
DBI
RPL22
MVB12B
RPL24
CCNG2
RPL39
RPL38
RPL36A
SESN1
SNAI1
B2M
AMEX60DD028405
MFSD14A
CDKN1B
RPL27
H2BC4
PPIF
RPL37A
RPS27A
Fibroblast
F
Homeostatic
Activated
Basal epidermis
Endothelial I
Endothelial II
Epidermal I
Epidermal II
Epidermal III
Epidermal IV
Fibroblast I
Fibroblast II
Fibroblast III
Fibroblast IV
Fibroblast V
Fibroblast VI
Fibroblast VII
Fibroblast VIII
Hematopoetic progenitor I
Hematopoetic progenitor II
Myeloid progenitor
RBC I
RBC II
Skeletal muscle
T-cell
G
Homeostatic
Activated
UMAP_1
UMAP_2
Epidermal
Small Secretory cell
Basal Keratinocytes
RBC I
RBC II
RBC III
RBC IV
T-cell I
T-cell II
T-cell III
T-cell IV
Potential MEP I
Potential MEP II
B-cell I
B-cell II
Myeloid progenitor
Lymphoid cell
Granulocyte
Monocyte
Monocyte II
Plasma cell
Myeloblast-like
Fibroblast
Skeletal Muscle
H
Homeostatic
Activated
Fibroblast
Epidermal
SSC
RBC
Potential MEP
Myeloid progenitor
Monocyte
B-cell
T-cell

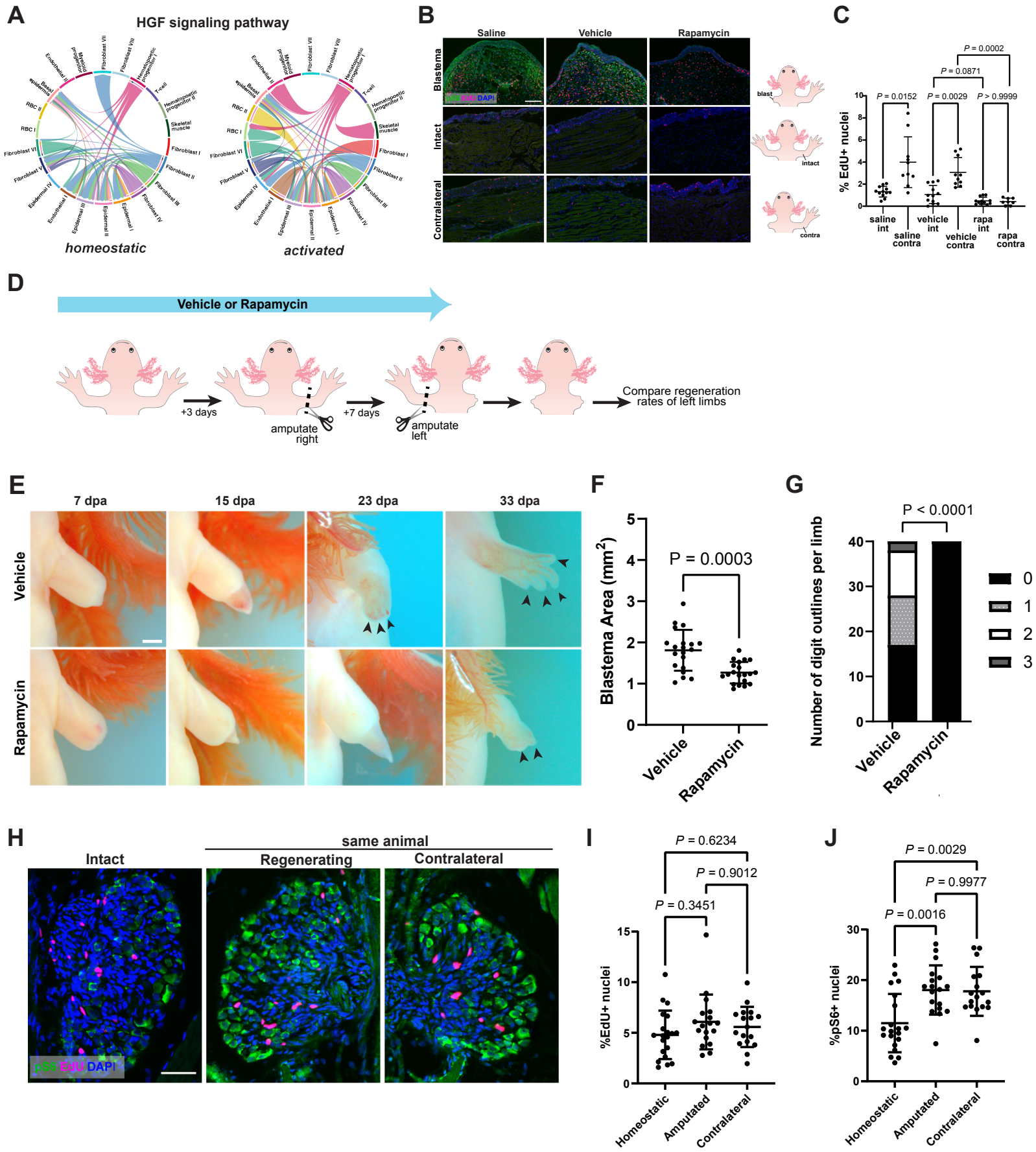
A
HGF signaling pathway
homeostatic
activated
B
Saline
Vehicle
Rapamycin
Blastema
Intact
Contralateral
pS6 EdU DAPI
blast
intact
contra
C
P = 0.0002
P = 0.0871
P = 0.0152
P = 0.0029
P > 0.9999
% EdU+ nuclei
saline int
saline contra
vehicle int
vehicle contra
rapa int
rapa contra
D
Vehicle or Rapamycin
+3 days
amputate right
+7 days
amputate left
Compare regeneration rates of left limbs
E
7 dpa
15 dpa
23 dpa
33 dpa
Vehicle
Rapamycin
F
P = 0.0003
Blastema Area (mm2)
Vehicle
Rapamycin
G
P < 0.0001
Number of digit outlines per limb
Vehicle
Rapamycin
0
1
2
3
H
same animal
Intact
Regenerating
Contralateral
pS6 EdU DAPI
I
P = 0.6234
P = 0.9012
P = 0.3451
%EdU+ nuclei
Homeostatic
Amputated
Contralateral
J
P = 0.0029
P = 0.9977
P = 0.0016
%pS6+ nuclei
Homeostatic
Amputated
Contralateral

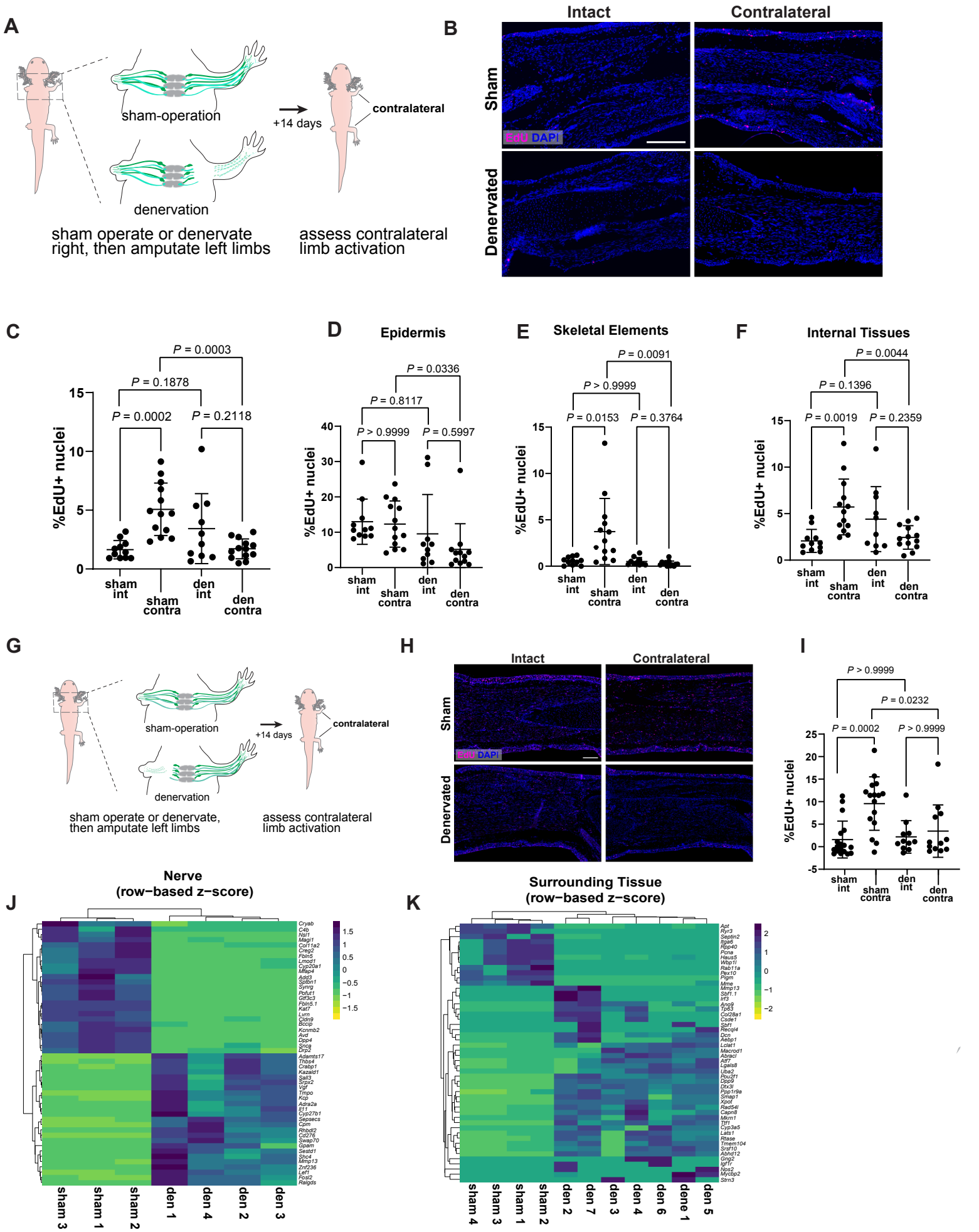
A
sham-operation
denervation
+14 days
contralateral
sham operate or denervate right, then amputate left limbs
assess contralateral limb activation
B
Intact
Contralateral
Sham
Denervated
EdU DAPI
C
%EdU+ nuclei
P = 0.0003
P = 0.1878
P = 0.0002
P = 0.2118
sham int
sham contra
den int
den contra
D
Epidermis
P = 0.0336
P = 0.8117
P > 0.9999
P = 0.5997
E
Skeletal Elements
P = 0.0091
P > 0.9999
P = 0.0153
P = 0.3764
F
Internal Tissues
P = 0.0044
P = 0.1396
P = 0.0019
P = 0.2359
G
sham-operation
denervation
+14 days
contralateral
sham operate or denervate, then amputate left limbs
assess contralateral limb activation
H
Intact
Contralateral
Sham
Denervated
EdU DAPI
I
%EdU+ nuclei
P > 0.9999
P = 0.0232
P = 0.0002
P > 0.9999
sham int
sham contra
den int
den contra
J
Nerve
(row−based z−score)
sham 3
sham 1
sham 2
den 1
den 4
den 2
den 3
K
Surrounding Tissue
(row−based z−score)
sham 4
sham 3
sham 1
sham 2
den 2
den 7
den 3
den 4
den 6
dene 1
den 5

Figure 4

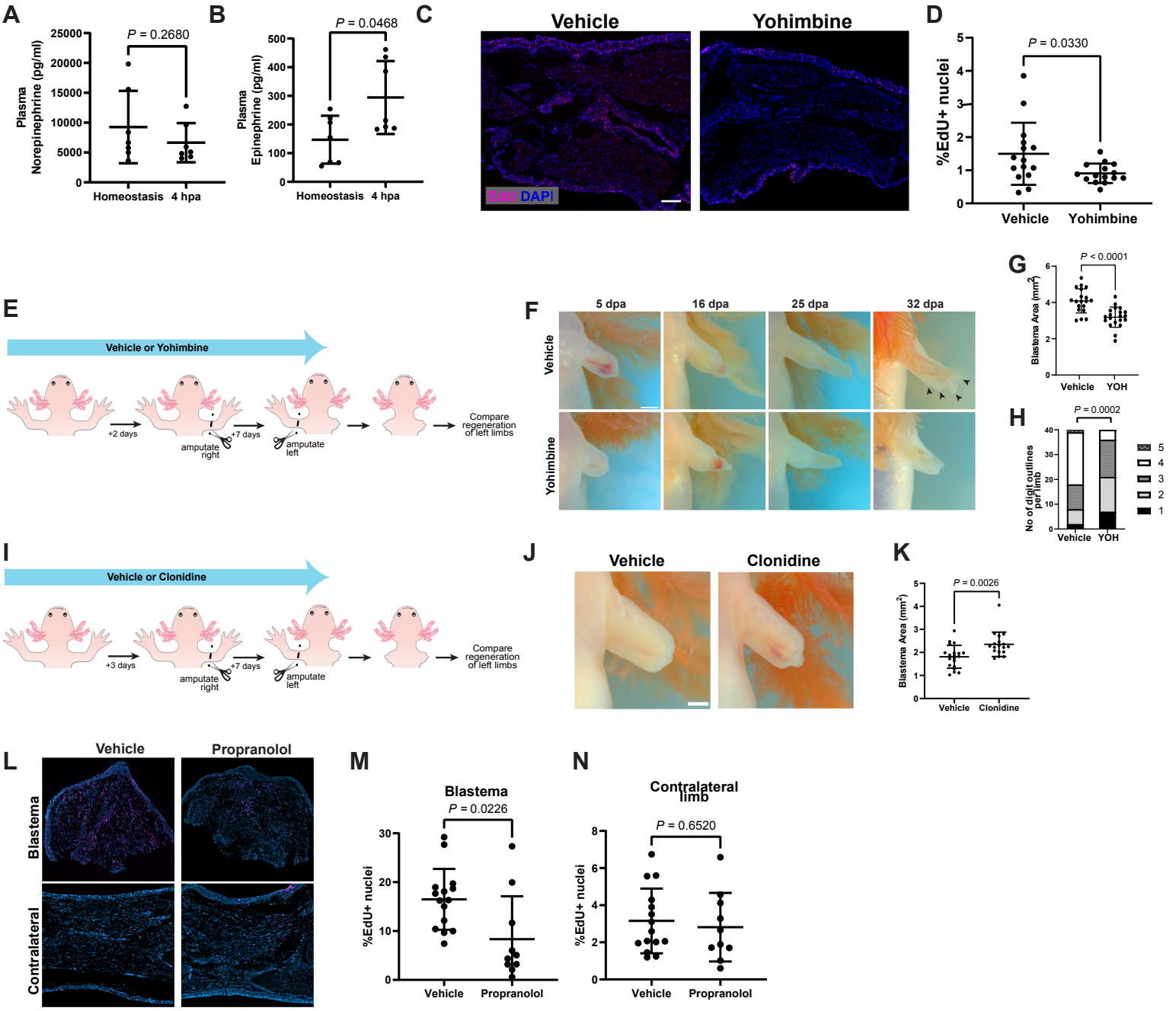
A
Plasma Norepinephrine (pg/ml)
P = 0.2680
Homeostasis
4 hpa
B
Plasma Epinephrine (pg/ml)
P = 0.0468
Homeostasis
4 hpa
C
Vehicle
Yohimbine
EdU DAPI
D
%EdU+ nuclei
P = 0.0330
Vehicle
Yohimbine
E
Vehicle or Yohimbine
+2 days
amputate right
+7 days
amputate left
Compare regeneration of left limbs
F
5 dpa
16 dpa
25 dpa
32 dpa
Vehicle
Yohimbine
G
Blastema Area (mm²)
P < 0.0001
Vehicle
YOH
H
No of digit outlines per limb
P = 0.0002
Vehicle
YOH
5
4
3
2
1
I
Vehicle or Clonidine
+3 days
amputate right
+7 days
amputate left
Compare regeneration of left limbs
J
Vehicle
Clonidine
K
Blastema Area (mm²)
P = 0.0026
Vehicle
Clonidine
L
Vehicle
Propranolol
Blastema
Contralateral
M
Blastema
%EdU+ nuclei
P = 0.0226
Vehicle
Propranolol
N
Contralateral limb
%EdU+ nuclei
P = 0.6520
Vehicle
Propranolol

Figure 5

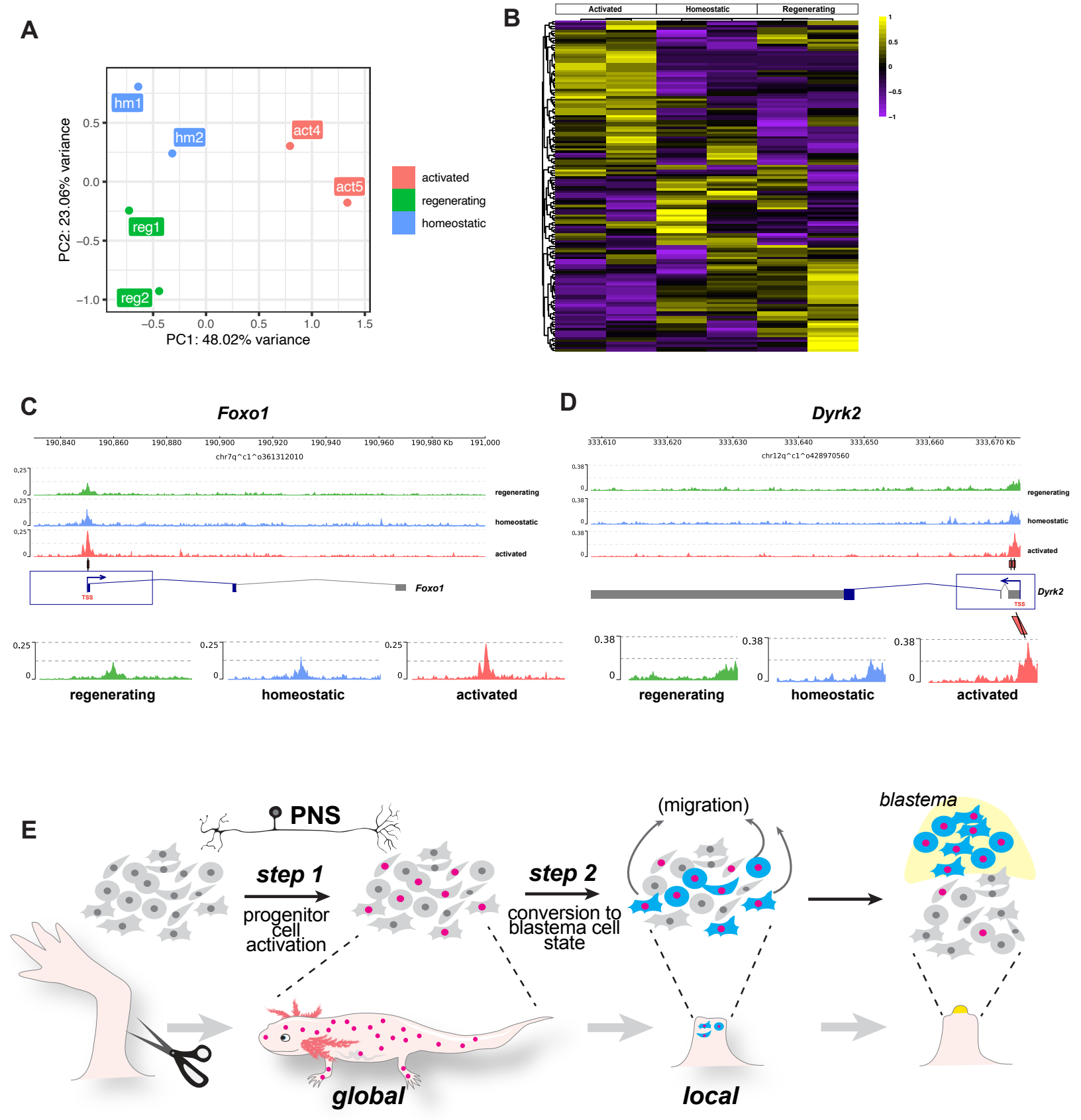
A
hm1
hm2
act4
act5
reg1
reg2
PC2: 23.06% variance
PC1: 48.02% variance
activated
regenerating
homeostatic
B
Activated
Homeostatic
Regenerating
C
Foxo1
chr7q^c1^o361312010
regenerating
homeostatic
activated
TSS
Foxo1
D
Dyrk2
chr12q^c1^o428970560
Dyrk2
E
PNS
step 1
progenitor cell activation
step 2
conversion to blastema cell state
(migration)
blastema
global
local

Figure 6

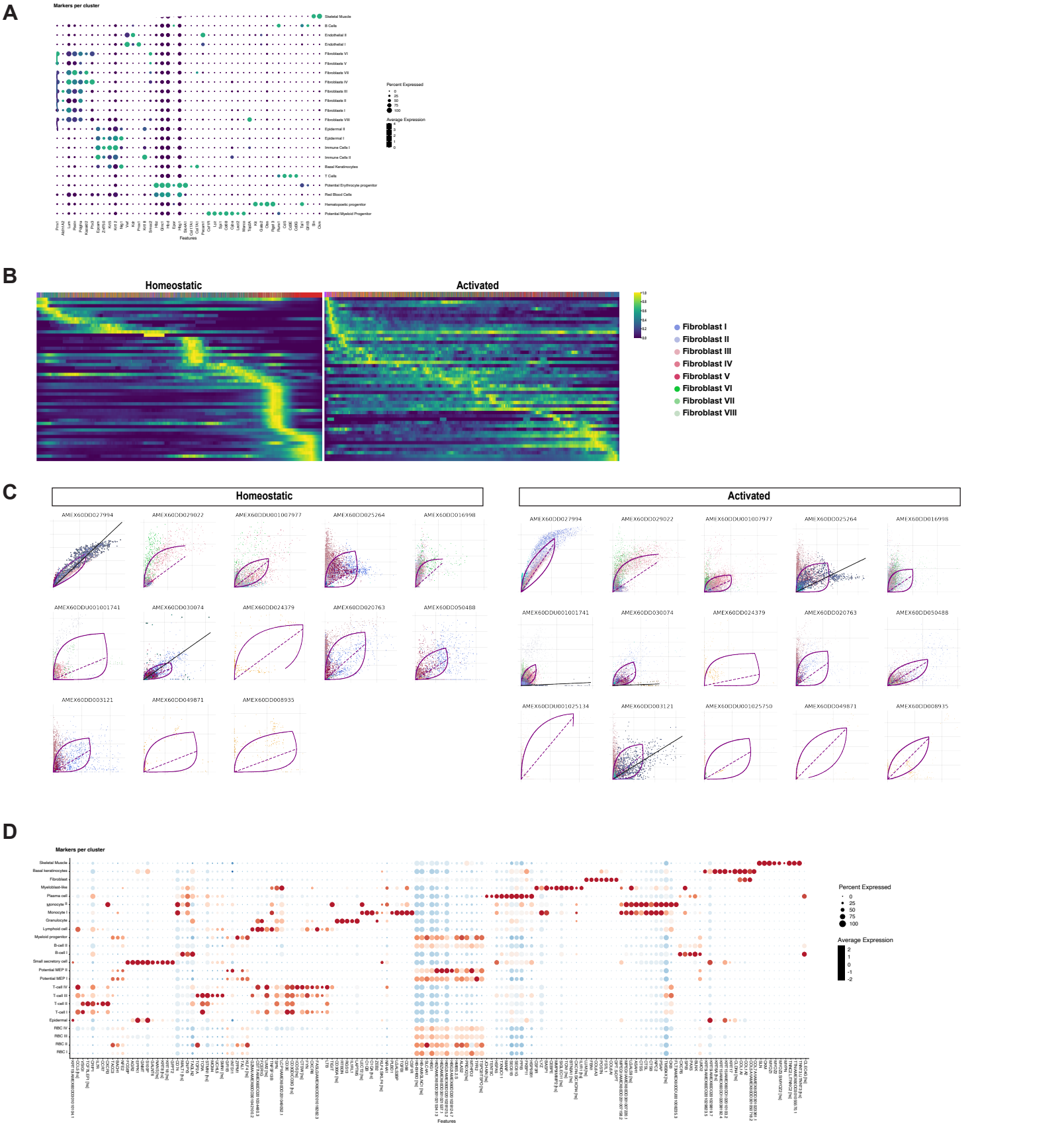

Figure S1, related to Figure 2

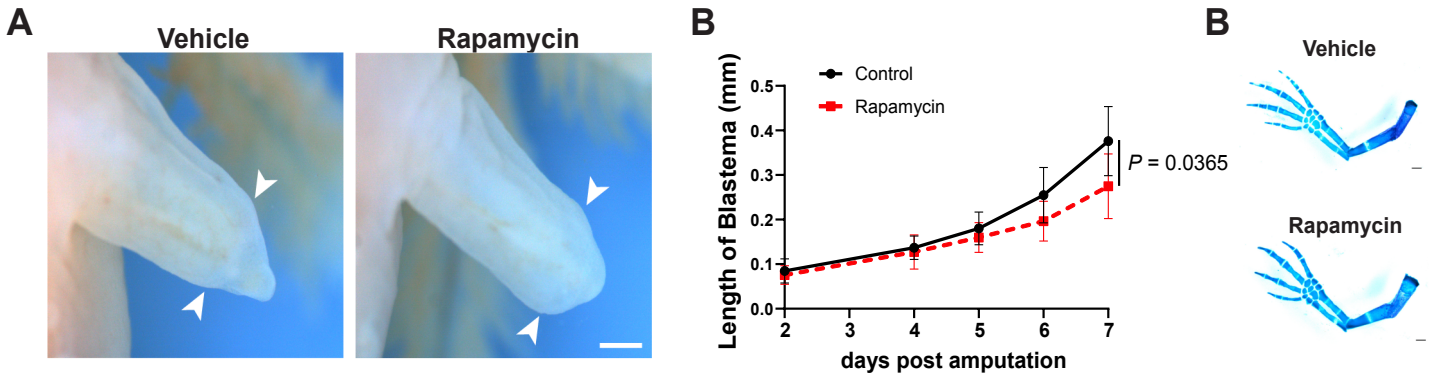

Figure S2, related to Figure 3

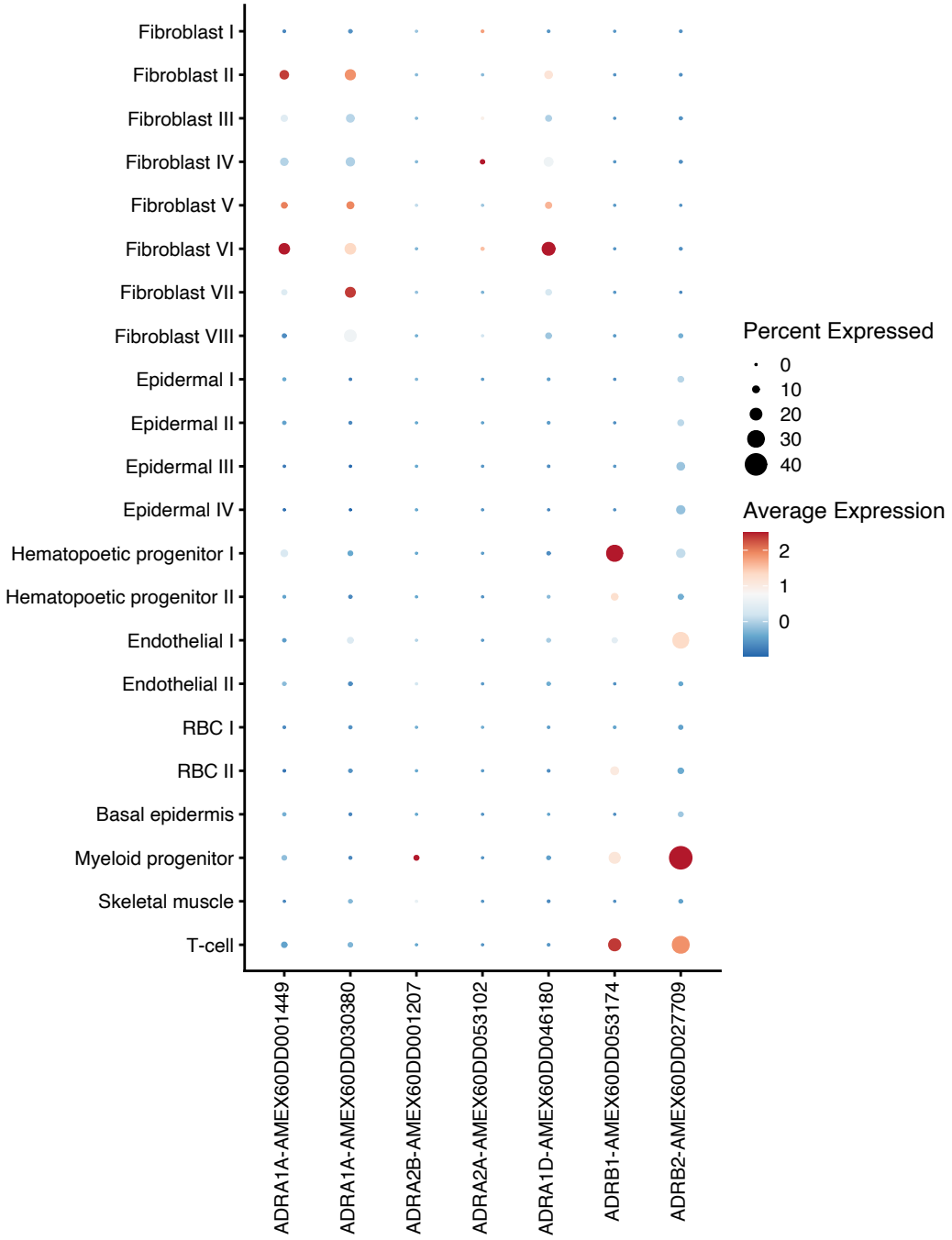

Figure S3, related to Figure 5

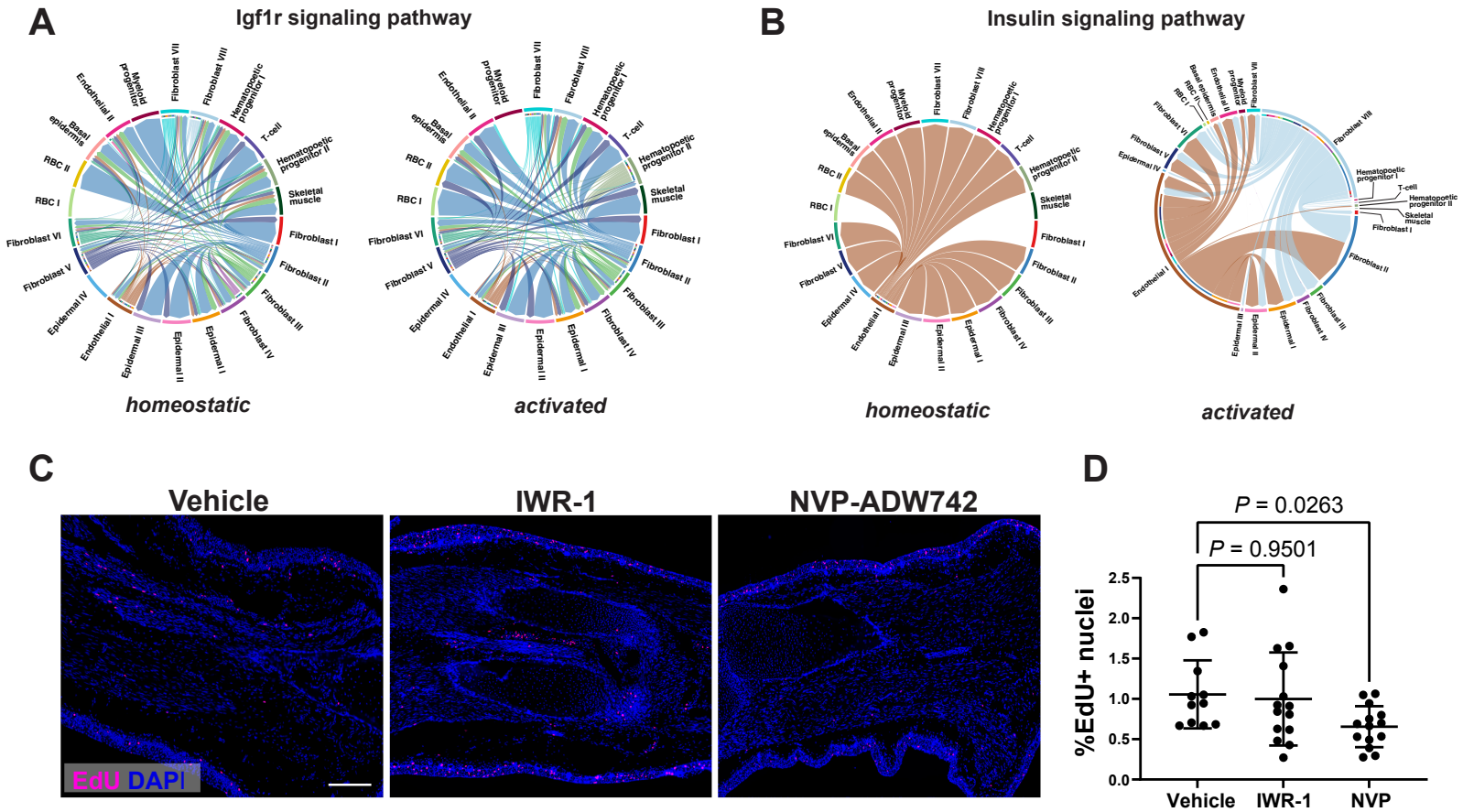

Figure S4, related to Figure 4